



ELSEVIER

Contents lists available at ScienceDirect

Journal of Computational Physics

www.elsevier.com/locate/jcp



A point-centered arbitrary Lagrangian Eulerian hydrodynamic approach for tetrahedral meshes



Nathaniel R. Morgan^{a,*}, Jacob I. Waltz^a, Donald E. Burton^a, Marc R. Charest^a,
Thomas R. Canfield^b, John G. Wohlbier^c

^a X-Computational Physics Division, Los Alamos National Laboratory, P.O. Box 1663, Los Alamos, NM, USA

^b Theoretical Division, Los Alamos National Laboratory, P.O. Box 1663, Los Alamos, NM, USA

^c Computer, Computational and Statistical Sciences Division, Los Alamos National Laboratory, P.O. Box 1663, Los Alamos, NM, USA

ARTICLE INFO

Article history:

Received 18 August 2014

Received in revised form 13 February 2015

Accepted 15 February 2015

Available online 24 February 2015

Keywords:

Lagrangian

Eulerian

Arbitrary Lagrangian Eulerian

Hydrodynamics

Point-centered

Godunov

Finite-element

Tetrahedron

ABSTRACT

We present a three dimensional (3D) arbitrary Lagrangian Eulerian (ALE) hydrodynamic scheme suitable for modeling complex compressible flows on tetrahedral meshes. The new approach stores the conserved variables (mass, momentum, and total energy) at the nodes of the mesh and solves the conservation equations on a control volume surrounding the point. This type of an approach is termed a point-centered hydrodynamic (PCH) method. The conservation equations are discretized using an edge-based finite element (FE) approach with linear basis functions. All fluxes in the new approach are calculated at the center of each tetrahedron. A multidirectional Riemann-like problem is solved at the center of the tetrahedron. The advective fluxes are calculated by solving a 1D Riemann problem on each face of the nodal control volume. A 2-stage Runge–Kutta method is used to evolve the solution forward in time, where the advective fluxes are part of the temporal integration. The mesh velocity is smoothed by solving a Laplacian equation. The details of the new ALE hydrodynamic scheme are discussed. Results from a range of numerical test problems are presented.

© 2015 The Authors. Published by Elsevier Inc. This is an open access article under the CC BY-NC-ND license (<http://creativecommons.org/licenses/by-nc-nd/4.0/>).

1. Introduction

Various point-centered hydrodynamic (PCH) Lagrangian approaches have been proposed [14,25,15,11,27,52,54,53,46,68,5]. The PCH approach is a spatially collocated method where the conservation equations for mass, momentum and total energy are solved on a control volume around the node, which is commonly termed the “dual grid”. Likewise, the strain is calculated on the same dual grid. The PCH approach differs from the staggered-grid hydrodynamic approach (SGH) [62,6,8,9,70] and the cell-centered hydrodynamic (CCH) approach [1,17,40,39,7,44,5]. The SGH approach solves the governing equations on staggered control volumes – the cell boundary and the dual grid respectively. The CCH approach is a collocated approach that solves the governing equations on a control volume that coincides with the cell boundary. Both CCH and SGH calculate the strain on the cell boundary. The CCH approach has been successfully applied to tetrahedral meshes in [5] and triangular meshes in [4]. With the compatible Lagrangian SGH approach [6,8], the strain calculation can be problematic on tetrahedral meshes (i.e. they are stiff). Scovazzi [53] performed analysis and presented numerical results demonstrating the compatible SGH approach does poorly on tetrahedral meshes. In contrast to both SGH and CCH, the PCH approach solves the governing

* Corresponding author.

E-mail address: nmorgan@lanl.gov (N.R. Morgan).

equations on the dual grid, which are arbitrary polyhedral control volumes that have many vertices. As a result, the dual grid has far more degrees of freedom to deform than a tetrahedral cell. The PCH approach offers some advantages over alternative hydrodynamic approaches for tetrahedral meshes.

A challenge with Lagrangian methods is the mesh can tangle on problems with large deformations. It is common to use the arbitrary Lagrangian Eulerian (ALE) [29] hydrodynamic approach on problems where the mesh deforms significantly. The benefit of the ALE approach is the mesh is able to move at an arbitrary velocity ranging from stationary (Eulerian limit) to the fluid velocity (Lagrangian limit). There are benefits to allowing the mesh to move at an arbitrary velocity. Two notable advantages are as follows. The robustness of the calculation is improved (i.e. the mesh is less likely to tangle), and the mesh can adapt to discontinuities. Recently, an ALE edge-based finite element (FE) Godunov PCH approach was proposed by Waltz et al. [67] for tetrahedral meshes. The approach in [67] is an extension of the Eulerian PCH approaches in [64,66] to ALE motion. The ALE approach in [67] includes the advective fluxes in the temporal integration, which differs from the Lagrange plus remap approach. The Lagrange plus remap approach performs ALE in three steps: (1) the mesh is moved according to the Lagrangian calculation, (2) the mesh is optimized, and (3) the physical quantities are advected from the old mesh to the new mesh (i.e. remap step). The ALE approach in [67] does not separate the ALE solution into a Lagrangian calculation followed by a remap step; rather, the advection is part of the temporal integration, which is termed “unsplit” in [67,65]. Unsplit ALE has been studied in various research efforts. Several notable examples of unsplit ALE are the CAVEAT research code [1] and the research by Boscheri et al. [5,4]. Other research efforts in unsplit advection include [24,47,49,48,51,28,23].

In this work, we build on the research in [64,66,67,46] and propose a new ALE edge-based FE PCH Godunov-like method, which reduces to the Lagrangian algorithm in [46] when the mesh velocity is equal to the fluid velocity. The new ALE algorithm discretizes the conservation equations with linear basis functions. The edge-based FE approach used here has many similarities to the finite volume approach. A unique feature of this algorithm is that all the fluxes are calculated at the tetrahedron center. A multidirectional Riemann-like problem is solved at the center of the tetrahedron, which yields a single Riemann-velocity and a single symmetric Riemann stress at the tetrahedron center. Likewise, the advective fluxes are calculated by solving an approximate 1D Riemann problem [16] on each control volume face connected to the center of the tetrahedron. Calculating fluxes at the center of the tetrahedron differs from the edge-based FE PCH Godunov methods that solve an approximate 1D Riemann problem on the edges [64,66–68,63,69]. The multidimensional Riemann-like problem used here is based on Lagrangian CCH work [17,40,39,7,44] and recent Lagrangian SGH work [36,37,41,38,45]. A 2-stage Runge–Kutta method is used to evolve the solution in time. The advective fluxes are included in the temporal integration so the new algorithm is an unsplit ALE algorithm.

The layout of the paper is as follows. The nomenclature used in the paper is discussed in Section 2. The governing equations are discussed in Section 3. The multidirectional Riemann-like problem at the tetrahedron center and the 1D approximate Riemann problem are discussed in Section 4. The details on the flow reconstruction are discussed in Section 5. The smoothing of the mesh velocity is discussed in Section 6. The computational procedure for implementing the ALE method is discussed in Section 7. Lastly, calculations of test problems are presented in Section 8.

2. Nomenclature

The nomenclature used in this paper follows the work in [7,6,44–46] and it is illustrated in Fig. 1. The density, velocity, mechanical stress, pressure, internal energy, and total energy are ρ , \mathbf{u} , $\boldsymbol{\sigma}$, p , e and j . The total energy is equal to the internal energy plus the kinetic energy, $j = e + \frac{1}{2}u^2$. The sound speed is c , and the shock speed is a and the shock direction is \mathbf{a} . Vectors and tensors are both denoted with bold font. Subscripts denote spatial locations and superscript letters denote temporal values such as n , $n + \frac{1}{2}$, or $n + 1$ respectively. The PCH approach is a spatially collocated method where the physical quantities are stored at the node, α . The neighboring nodes to α are denoted as β and they are connected by an edge, e . The conservation equations are solved on a control volume (CV) that encircles the node α , which is termed the dual grid or the nodal control volume.

The nodal control volumes are decomposed into smaller segments, where each segment is termed an iota and denoted with a subscript i . The motivation for the decomposition is that the control volume for the multidirectional Riemann-like problem will be constructed from the iota surfaces inside a tetrahedron z , which is denoted as $i \in z$. In 3D, an iota on the nodal control volume surface is made of 4 points: (1) the center of the face on the left, (2) the cell center of the tetrahedron cell, (3) the center of the face on the right, and (4) the middle of the edge. The outward surface area normal of the iota is a quadrilateral surface, and it is denoted as \mathbf{S}_i . The surface unit normal vector of the iota face is denoted with a lower case letter, \mathbf{s}_i . All the iota surfaces around the node is $i \in \alpha$.

In this work, the fluxes in the conservation equations are calculated at the center of the tetrahedron, z . The fluxes are calculated by solving two different Riemann-like problems – an approximate 1D Riemann problem and a multidirectional Riemann-like problem respectively. The advective fluxes are calculated by solving a 1D Riemann problem on each segment of the nodal control volume surface, i , inside the tetrahedron. The 1D Riemann advective fluxes are denoted with a subscript i and a superscript $*$. The Riemann velocity for the tetrahedron center and the Riemann stresses in the corners of the tetrahedron center are calculated by solving a multidirectional Riemann-like problem using every segment of the nodal control volume surface, i , inside the tetrahedron. Every segment inside the tetrahedron is denoted as $i \in z$. The Riemann velocity is denoted with a subscript z and a superscript $*$. The corresponding Riemann stresses are denoted with a subscript

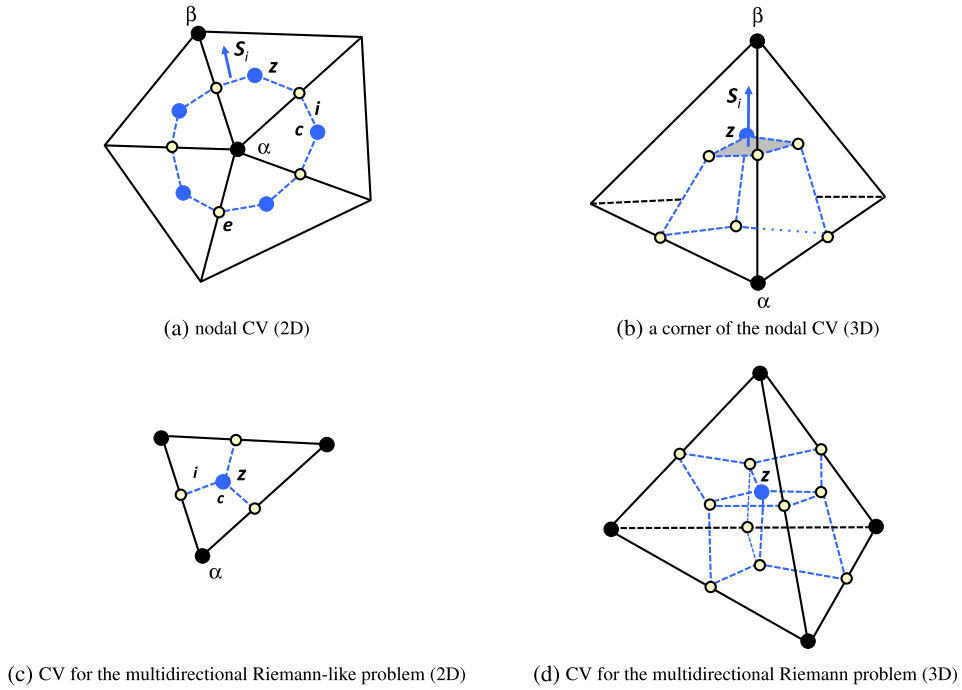


Fig. 1. The point centered hydrodynamic approach solves the conservation equations for mass, momentum, and total energy on a control volume around the node α . Caption (a) illustrates the entire nodal control volume for a 2D case (blue dashed line), and caption (b) only shows a single corner of the nodal control volume in 3D for simplicity purposes. The neighboring nodes are denoted as β . The cell center of the tetrahedron is z . The nodal control volume is subdivided into smaller segments that are termed an iota and they are denoted as i . The surface area normal vector of an iota is S_i . The iota surface area vectors are equal in magnitude and opposite in direction along an edge. A multidirectional Riemann-like problem is solved at the cell center z . The control volume (CV) for the multidirectional Riemann-like problem is made from every iota surface inside a tetrahedron cell, $i \in z$. Caption (c) shows the 6 iota surface areas used to make the CV to solve the 2D multidirectional Riemann-like problem. For a triangle, the iota surface extends from the edge e to the cell center z , which is shown with a dashed line. Caption (d) shows the 12 iota surface areas used to make the CV to solve the 3D multidirectional Riemann problem on the iota surfaces. The inputs to both Riemann problems are the quantities in the tetrahedron corner, c . Fig. 2 provides another diagram to illustrate the concept behind the multidimensional Riemann-like problem. (For interpretation of the references to color in this figure legend, the reader is referred to the web version of this article.)

c and a superscript $*$. The multidirectional Riemann-like problem uses the quantities in all 4 corners, whereas, the 1D Riemann problem uses only two corner values. The quantities in a tetrahedron corner are denoted with a subscript c . The corner quantities are calculated by projecting the quantity from the nodes to the tetrahedron center via a linear Taylor Series expansion and a limited gradient. The projected velocity from a node to the cell center is \mathbf{u}_c where the subscript c denotes the corner. The Riemann velocity from the multidirectional Riemann-like problem is \mathbf{u}_z^* and the corresponding Riemann stress in the tetrahedron corner is σ_c^* .

3. Governing equations

The governing equations for mass, momentum, and total energy evolution are written in terms of an arbitrary mesh velocity, \mathbf{w} .

$$\frac{d}{dt} \int_V \rho dV + \oint_{\partial V} (d\mathbf{S} \cdot \rho(\mathbf{u} - \mathbf{w})) = 0 \tag{1}$$

$$\frac{d}{dt} \int_V \rho \mathbf{u} dV + \oint_{\partial V} (d\mathbf{S} \cdot \rho \mathbf{u}(\mathbf{u} - \mathbf{w})) = \oint_{\partial V} (d\mathbf{S} \cdot \boldsymbol{\sigma}) \tag{2}$$

$$\frac{d}{dt} \int_V \rho j dV + \oint_{\partial V} (d\mathbf{S} \cdot \rho j(\mathbf{u} - \mathbf{w})) = \oint_{\partial V} (d\mathbf{S} \cdot \boldsymbol{\sigma} \cdot \mathbf{u}) \tag{3}$$

where $d\mathbf{S}$ is an infinitesimally small surface area, V is the volume, the density is ρ , \mathbf{u} is the velocity, j is the specific total energy, and $\boldsymbol{\sigma}$ is the stress. In the Eulerian limit, the mesh velocity, \mathbf{w} is equal to zero. Likewise, in the Lagrangian limit the mesh velocity is equal to the fluid velocity, $\mathbf{u} = \mathbf{w}$. The conservation equations are discretized using the edge-based FE approach. In addition, the algorithm is derived such that it satisfies a series of key design objectives. The first design goal for

the new algorithm is it must be conservative by construction. Specifically, we seek to conserve mass, momentum, and total energy for any mesh velocity and any mesh resolution. The second design goal for the new algorithm is it should ensure a stable, monotone solution. The Riemann problems must add the appropriate amount of dissipation at discontinuities so that the solution does not generate spurious oscillations. The last design goal for the new algorithm is it should minimize dissipation on smooth flows. Excessive dissipation on smooth flows can have a deleterious impact on a calculation. These design goals will be referenced in this paper.

3.1. Discrete governing equations

The governing analytic equations are discretized using the edge-based finite element (FE) approach discussed in [64,66,67,46]. Using this approach, the discrete equations take the form of

$$\frac{\Delta(\mathbf{U}_\alpha V_\alpha)}{\Delta t} = \sum_{i \in \alpha} (\mathbf{S}_i \cdot \mathcal{F}_i) \quad (4)$$

where U_α are the conserved unknowns vector at the node and \mathbf{S}_i is the surface area normal vector of the iota and \mathcal{F}_i are the corresponding fluxes on an iota surface. The conserved unknowns vector in Eq. (4) is

$$\mathbf{U} = \begin{bmatrix} \rho \\ \rho \mathbf{u} \\ \rho j \end{bmatrix} \quad (5)$$

Next, the surface area normal vector, \mathbf{S}_i , is calculated using the linear basis functions, $N(x)$, and it is given by

$$\mathbf{S}_i = \int_{V(z)} (N_\alpha \nabla N_\beta - N_\beta \nabla N_\alpha) dV \quad (6)$$

The details on the derivation of the surface area normal vector are provided in [64,67]. Next, the fluxes in Eq. (4) are

$$\mathcal{F}_i = \begin{bmatrix} 0 \\ \sigma_c^* \\ \sigma_c^* \cdot \mathbf{u}_z^* \end{bmatrix} + \begin{bmatrix} \rho_i^* (\mathbf{w}_i - \mathbf{u}_i) \\ \rho_i^* \mathbf{u}_i^* (\mathbf{w}_i - \mathbf{u}_i) \\ \rho_i^* j_i^* (\mathbf{w}_i - \mathbf{u}_i) \end{bmatrix} + \mathbf{S}_i a_i \begin{bmatrix} \rho_i^* - \rho_c \\ \rho_i^* \mathbf{u}_i^* - \rho_c \mathbf{u}_c \\ \rho_i^* j_i^* - \rho_c j_c \end{bmatrix}. \quad (7)$$

Substituting the fluxes above into Eq. (4) produces a discrete approximation of the analytic equations for mass, momentum, and total energy evolution (Eqs. (1), (2), and (3)). The discrete fluxes use the Riemann solution values, which are denoted with a superscript *. The Riemann values in the first column, σ_c^* and \mathbf{u}_z^* , are found a solving a multidirectional Riemann-like problem at the tetrahedron center. The second and third columns are advective and dissipative fluxes that transport mass, momentum, and total energy through the nodal control volume facets (termed an iota). The advective and dissipative fluxes are calculated by solving a 1D Riemann problem on each iota surface at the tetrahedron center. The details on the multidirectional Riemann-like problem and the 1D Riemann problem are discussed in greater detail in Section 4.

The fluxes in Eq. (7) are intentionally separated into three columns. The fluxes in the first column correspond to pure Lagrangian motion, so the solution is pure Lagrangian when the second and third columns are equal to zero. The fluxes in the second and third column account for ALE motion, where the solution is pure Eulerian when the mesh velocity, \mathbf{w}_i , is equal to zero. The dissipative fluxes in the third column are essential for numerical stability, and they are used in other PCH edge-based FE approaches [64,66,67,46]. The dissipative fluxes correspond to the Rusanov fluxes [16] and they are used to shift the numerical approximation from an unstable central difference discretization toward a first-order upwind discretization that is stable and monotone. Section 4.3 provides the details on how the dissipative fluxes shift the solution toward a first-order upwind discretization. The dissipative fluxes also remove a particular volume change error that exists in the PCH discretization of the volume evolution equation [46], and the details are provided in Section 4.4. The amount of dissipation added to the calculation from the dissipative fluxes is a function of the shock speed, a , and the difference between the 1D approximate Riemann solution and the corner value. The dissipation from the dissipative field will be equal to zero in the limit of a zero mesh size or if the flow is linear with a linear reconstruction of the flow field.

Next, the decomposition of the fluxes (Eq. (7)) into three columns is useful for seeing the difference between the ALE approach in this paper and a Lagrange plus remap operator split approach. In a Lagrange plus remap approach, the advective fluxes are not included in the temporal integration, likewise, the dissipative fluxes are not required because the advective fluxes are calculated using upwind values of the unknowns (e.g. ρ , $\rho \mathbf{u}$, ρj). In this work, every flux is included in the temporal integration and the fluxes are based on Riemann solutions.

3.2. Temporal discretization

The solution is integrated forward in time using the 2-stage Runge–Kutta method. The first step is to calculate the mesh velocity at time level n using the fluid velocity, \mathbf{u} . The mesh velocity is found by solving a Laplacian equation (Section 6)

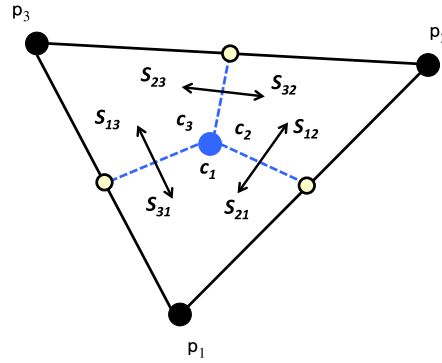


Fig. 2. A 2D example is provided above to illustrate the multidimensional Riemann-like problem at the cell center. The iota surface area vectors, \mathbf{S}_i are shown, where the subscripts on the surface vector indicate the iota face and the direction. For example, subscript 12 is an iota surface with a normal vector pointing from corner 1 to corner 2. For a triangle, there are 6 iota surface areas. The inputs to the multidimensional Riemann-like problem are the corner values, c . The Riemann velocity at z is found by enforcing conservation of momentum.

that smooths the mesh velocity field. The next step is to integrate in time the solution from n to $n + 1/2$, where the right hand side of the discrete equations is at time level n . The unknowns vector (Eq. (5)) is integrated temporarily as

$$(\mathbf{U}_\alpha V_\alpha)^{n+1/2} = (\mathbf{U}_\alpha V_\alpha)^n + \frac{\Delta t}{2} \sum_{i \in \alpha} (\mathbf{S}_i \cdot \mathcal{F}_i)^n \tag{8}$$

likewise, the mesh position at $n + 1/2$ is given by

$$\mathbf{x}_\alpha^{n+1/2} = \mathbf{x}_\alpha^n + 1/2 \Delta t \mathbf{w}_\alpha^n. \tag{9}$$

The thermodynamic variables and the fluxes are calculated using the information at $n + 1/2$. In addition, the mesh velocity at $n + 1/2$ is calculated. The second step is to integrate the solution from n to $n + 1$, where the right hand side of the discrete equation is at time level $n + 1/2$.

$$(\mathbf{U}_\alpha V_\alpha)^{n+1} = (\mathbf{U}_\alpha V_\alpha)^n + \Delta t \sum_{i \in \alpha} (\mathbf{S}_i \cdot \mathcal{F}_i)^{n+1/2} \tag{10}$$

and the mesh position at $n + 1$ is

$$\mathbf{x}_\alpha^{n+1} = \mathbf{x}_\alpha^n + \Delta t \mathbf{w}_\alpha^{n+1/2}. \tag{11}$$

The time integration process is repeated until the final time is reached.

4. Riemann problems

The new PCH ALE approach solves two Riemann problems at the center of each tetrahedron. The motivation for using two Riemann problems is as follows. In the Lagrangian limit, the algorithm should produce robust mesh motion. We choose to use a multidirectional Riemann-like problem because they have excellent mesh robustness properties when compared to Lagrangian algorithms that solve a 1D Riemann problem on the control volume faces such as the approach in [1]. Specifically, spurious vorticity errors in a Lagrangian CCH calculation can grow to unacceptable levels in a calculation when using a traditional 1D Riemann solution [21]. Another nice feature of the multidirectional Riemann-like problems is a single Riemann velocity can be found for the vertices of the nodal control volume (i.e. the tetrahedron center). Next, an ALE scheme must support advection so a separate 1D Riemann problem is solved. The advection is through the iota surfaces at the center of the tetrahedron, so it is natural to solve a 1D Riemann problem on each iota face. The details on the two Riemann problems are provided in the two following subsections.

4.1. Multidirectional Riemann-like problem

The concept of using a multidirectional Riemann-like problem originated in recent Lagrangian CCH work [17,40,39,7,44] and recent Lagrangian SGH work [36,37,41,38,45]. The first multidirectional Riemann-like problem was proposed by Despres and Mazeran [17]. Maire and various authors [40,39] extended the work in [17] and proposed a new multidirectional Riemann-like approach that had improved mesh robustness properties. Burton et al. [7] extended the seminal works in [17,40,39] and proposed another robust multidirectional Riemann-like approach that was suitable for materials with strength. A nice feature of the approach in [7] is the resulting Riemann stress tensors in the control volume corners is symmetric. The approach in [7] was also successfully applied to contact surfaces in Lagrangian CCH [44], applied to Lagrangian SGH [45], and applied to Lagrangian PCH [46]. In this work, we use the approach in [7] with PCH ALE.

The concept behind the multidirectional Riemann-like problem is to apply a Riemann jump relation to each iota surface inside a tetrahedron (Fig. 2) and then solve for a single Riemann velocity, \mathbf{u}_z^* , that ensures conservation of momentum and total energy. The Riemann jump relation from [7] is

$$\mu_c (\mathbf{u}_z^* - \mathbf{u}_c) |\mathbf{a}_c \cdot \mathbf{S}_i| = \mathbf{S}_i \cdot (\boldsymbol{\sigma}_c^* - \boldsymbol{\sigma}_c) \tag{12}$$

where \mathbf{a}_c is a unit vector in each corner that points in the direction that the shock is traveling. The term $|\mathbf{a}_c \cdot \mathbf{S}_i|$ rotates the Riemann jump relation from the reference frame of the shock into the reference frame of the mesh. For a 1D flow on a 1D mesh, $|\mathbf{a}_c \cdot \mathbf{S}_i| = \|\mathbf{S}_i\|$ (i.e. the surface area), which yields the canonical 1D Riemann problem which states the jump in pressure is proportional to the jump in velocity. The shock direction in a corner is assumed to be in the direction of the velocity difference between the tetrahedron corner and the tetrahedron average velocity. The Riemann jump relation in Eq. (12) is applied to each iota surface, i inside the tetrahedron. In this work, the surface area normals \mathbf{S}_i (Eq. (6)) are derived from the FE basis functions. There are a total of 12 surface area normals in a tetrahedron. The surface area normals are equal in area and opposite in direction on each edge. Likewise, there are a total of 4 corners in a tetrahedron. The corner values in the Riemann jump relation are constructed by spatially reconstructing the flow variables over the nodal CV using a linear Taylor-Series expansion and a limited gradient. For reference, the 1st-order approach would just use the nodal values (i.e. $\mathbf{u}_c = \mathbf{u}_\alpha$). The shock impedance is approximated as $\mu_c = \rho_c(c + b_1 \delta u_c)$ [20], where the quantity in the parentheses is an approximation of the shock velocity. In this work, the shock velocity is assumed to be a linear function of the acoustic wave speed, c , and a linear coefficient b_1 that is a material dependent value. The linear coefficient can be found for a range of materials including metals in Cooper [13], Zukas and Walters [72], and Marsh [43]. The velocity difference in the shock impedance is defined as

$$\delta u_c = \left\| \mathbf{u}_c - \frac{1}{4} \sum_{p \in Z} \mathbf{u}_p \right\|. \tag{13}$$

Next, the Riemann velocity at the tetrahedron center is founded by enforcing momentum conservation. Momentum conservation requires the summation of all the forces inside the tetrahedron to be equal to zero. It is an algorithmic design goal to be conservative.

$$\sum_{i \in Z} \mathbf{S}_i \cdot \boldsymbol{\sigma}_c^* = 0 \tag{14}$$

The Riemann velocity at the tetrahedron center is found via solving the system of the equations involving the Riemann jump equations on each segment, \mathbf{S}_i , and enforcing momentum conservation at the tetrahedron center. The Riemann velocity at z is

$$\mathbf{u}_z^* = \frac{\sum_{i \in Z} (\mu_c |\mathbf{a}_c \cdot \mathbf{S}_i| \mathbf{u}_c - \mathbf{S}_i \cdot \boldsymbol{\sigma}_c)}{\sum_{i \in Z} \mu_c |\mathbf{a}_c \cdot \mathbf{S}_i|} \tag{15}$$

The Riemann velocity above is used in the total energy flux (Eq. (7)) and it is used to calculate the total surface force on an iota, $\mathbf{S}_i \cdot \boldsymbol{\sigma}^*$. The total surface force (mechanical plus viscous contributions) is found by substituting the Riemann velocity (Eq. (15)) into the Riemann jump equation (Eq. (12)). The Riemann force on a segment of the nodal control volume surface is

$$\mathbf{S}_i \cdot \boldsymbol{\sigma}^* = \mathbf{S}_i \cdot \boldsymbol{\sigma}_c + \mu_c (\mathbf{u}_z^* - \mathbf{u}_c) |\mathbf{a}_c \cdot \mathbf{S}_i| \tag{16}$$

The Riemann force is used in the discrete governing equations for the momentum and the total energy evolution (Eqs. (4) and (7)). The total energy will be conserved with the Riemann forces above because the total energy fluxes sum to zero around the cell; in other words, $\sum_{i \in Z} (\mathbf{S}_i \cdot \boldsymbol{\sigma}^* \cdot \mathbf{u}_z^*) = \sum_{i \in Z} (\mathbf{S}_i \cdot \boldsymbol{\sigma}^*) \cdot \mathbf{u}_z^* = 0$. Conserving total energy is a design goal of the algorithm.

4.2. 1D Riemann problem

A 1D approximate Riemann problem is solved on each iota surface using the two corner values along the edge. The 1D Riemann problem is

$$\mathbf{f}_i^U = \mathbf{s} a_i (\mathbf{U}_i^* - \mathbf{U}_c), \tag{17}$$

where \mathbf{f}_i^U denotes the flux vector on the iota surface and the corner quantities are $\mathbf{U}_c = [\rho_c, \rho_c \mathbf{u}_c, \rho_c j_c]$ and the 1D Riemann solution is $\mathbf{U}_i^* = [\rho_i^*, \rho_i^* \mathbf{u}_i^*, \rho_i^* j_i^*]$. The flux vector, \mathbf{f}_i^U , is the third column in Eq. (7). The shock speed on the iota surface, i , is the maximum value of the two corner values in the 1D Riemann problem, $a_i = \max(a_{c(\alpha)}, a_{c(\beta)})$, which is based on work by Davis [16]. The subscripts $c(\alpha)$ and $c(\beta)$ denote the two corner values associated with the iota surface, i . The shock speed is defined as $a_c = c_c + b_1 \|\mathbf{u}_{c(\beta)} - \mathbf{u}_{c(\alpha)}\|$. The shock speed here follows the definition for the shock speed

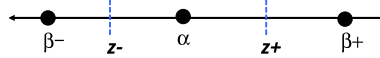


Fig. 3. A 1D mesh is provided to illustrate the nomenclature used in the stability and monotonicity analysis and the volume change error analysis. The dashed blue line denote the edges of the nodal control volume. (For interpretation of the references to color in this figure legend, the reader is referred to the web version of this article.)

used in the multidirectional Riemann-like problem discussed in the previous subsection. The approximate Riemann solution is found by enforcing conservation across the iota surface,

$$\sum_{c \in i} \mathbf{S}_i \cdot \mathbf{s} a_i (\mathbf{U}_i^* - \mathbf{U}_c) = 0. \tag{18}$$

Conservation is a design goal for the algorithm. The 1D approximate Riemann solution on the iota surface is simply

$$\mathbf{U}_i^* = \frac{1}{2} (\mathbf{U}_{c(\alpha)} + \mathbf{U}_{c(\beta)}). \tag{19}$$

The 1D Riemann solutions are used in both the advective fluxes and the dissipative fluxes (Eq. (7)). The importance of the dissipative fluxes is discussed in the following two sections.

4.3. Stability and monotonicity

The PCH approach uses a central difference approximation for a hyperbolic equation and for the volume change equation. A central difference approximation is not numerically stable for these equations. The additional dissipative fluxes shift the solution in the upwind direction, which stabilizes the scheme and removes a volume change error. The discussion below will focus on the importance of the dissipative fluxes for stabilizing the advection. The details on a particular volume change error are provided in [46] and they are briefly discussed in the proceeding subsection. Fig. 3 illustrates the nomenclature used in the stability and monotonicity analysis and the volume change error analysis.

The importance of the dissipative fluxes can be seen by analyzing the 1D linear advection equation, $\frac{dU}{dt} + a \frac{dU}{dx} = 0$. In this equation, U is some unknown quantity and the wave speed, a , is constant and greater than 0. For this 1D analysis, a first-order reconstruction will be used. The discretized equation in the Eulerian reference frame is

$$\frac{\Delta(U_\alpha V_\alpha)}{\Delta t} + a (U_{z+}^* - U_{z-}^*) \|\mathbf{S}\| = \underbrace{a (U_{z+}^* - U_\alpha) \|\mathbf{S}\| + a (U_{z-}^* - U_\alpha) \|\mathbf{S}\|}_{dissipation} \tag{20}$$

where the terms on the right side of Eq. (20) are the additional Rusanov dissipation terms. The equation above can be simplified to

$$\frac{\Delta U_\alpha}{\Delta t} + a \frac{(U_{z+}^* - U_{z-}^*)}{L_\alpha} = a \frac{(U_{z+}^* - 2U_\alpha + U_{z-}^*)}{L_\alpha} \tag{21}$$

where the volume and the surface area are replaced by the nodal control volume length, L , because $V = L\|\mathbf{S}\|$. The 1D Riemann solutions at the iota surfaces are $U_{z+}^* = 1/2(U_{\beta+} + U_\alpha)$ and $U_{z-}^* = 1/2(U_\alpha + U_{\beta-})$ respectively. Substituting the Riemann solutions into Eq. (21) gives

$$\frac{\Delta U_\alpha}{\Delta t} + a \frac{(U_{\beta+} - U_{\beta-})}{2L_\alpha} = \frac{1}{2} a L_\alpha \frac{(U_{\beta+} - 2U_\alpha + U_{\beta-})}{L_\alpha^2} \tag{22}$$

or

$$\frac{\Delta U_\alpha}{\Delta t} + a \frac{(U_\alpha - U_{\beta-})}{L_\alpha} = 0. \tag{23}$$

The discrete equation reduces to the canonical central difference approximation of the first derivative plus a discrete approximation of $\frac{d^2U}{dx^2}$ on the right side. The discrete second derivative term switches the discretization in the upwind direction, which is stable and will produce monotone solutions. The dissipative fluxes are essential for satisfying the design goal of a stable approach that produces monotone solutions.

4.4. A volume change error

A particular volume change error occurs in Lagrangian PCH that must be addressed for stable solutions on shock problems. The volume change error discussed in this section arises from a particular null mode. The term null mode is used to describe the scenario where a node or a set of nodes can move without generating a volume change in the control volume. In this section we discuss a unique and highly undesirable null mode that occurs in pure Lagrangian PCH around shocks. It will be shown in this section that this undesirable null mode can be removed by including the additional Rusanov

dissipative terms. A more thorough derivation and discussion is provided in [46]. Addressing this null mode is of pivotal importance because the PCH approach proposed here must be capable of modeling shock problems in the Lagrangian limit, in the Eulerian limit, and in the ALE reference frame.

The Lagrangian PCH approach calculates the volume change using either a lumped volume approach (i.e. $V_\alpha = \sum_{z \in \alpha} \frac{1}{4} V_z$) or via the mesh velocity at the edge center, $\frac{\Delta V_\alpha}{\Delta t} = \sum_{i \in \alpha} \mathbf{S}_i \cdot \mathbf{w}_e$. These two approaches do not correctly calculate the change in the volume when a node moves; in other words, a single node can move and there will be no volume change. In 1D it is easy to demonstrate the volume change null mode error. In this analysis, we assume the mesh velocity is equal to the fluid velocity $\mathbf{w} = \mathbf{u}$. Please consider the case where a single node moves at a velocity, u_α , and the neighboring nodes are stationary (e.g. $u_{\beta+} = u_{\beta-} = 0$). For the lumped volume approach, the 1D volume change is

$$\frac{\Delta V_\alpha^{1D}}{\Delta t} = \frac{V_\alpha^{n+1} - V_\alpha^n}{\Delta t} = \frac{\frac{1}{2}(x_{\beta+}^{n+1} - x_{\beta-}^{n+1}) - \frac{1}{2}(x_{\beta+}^n - x_{\beta-}^n)}{\Delta t} = 0 \quad (24)$$

The volume change is zero because the neighboring nodes to α are stationary so $x_{\beta+}^n = x_{\beta+}^{n+1}$ and $x_{\beta-}^n = x_{\beta-}^{n+1}$. The volume change will be zero for any nodal displacement at α . The volume change equation based on the edge velocity is also equal zero for this 1D test case.

$$\frac{\Delta V_\alpha^{1D}}{\Delta t} = \sum_{i \in p} \mathbf{S}_i \cdot \mathbf{u}_e = \frac{1}{2}(\mathbf{u}_{\beta+}^{n+1/2} + \mathbf{u}_\alpha^{n+1/2}) - \frac{1}{2}(\mathbf{u}_\alpha^{n+1/2} + \mathbf{u}_{\beta-}^{n+1/2}) = \frac{1}{2}(\mathbf{u}_{\beta+}^{n+1/2} + \mathbf{u}_{\beta-}^{n+1/2}) = 0 \quad (25)$$

As before, the volume change is zero because the neighboring nodes are stationary, $\mathbf{u}_{\beta+}^{n+1/2} = \mathbf{u}_{\beta-}^{n+1/2} = 0$. The node α can move at any velocity and there will be no volume change. The Lagrangian PCH approach has a highly undesirable volume change error that must be addressed.

The volume change error discussed in this section is created by evolving the nodal control volumes at the incorrect velocity. The nodal control volumes should move at the contact wave speed, u_z^* . The research effort in [2] applied a Lagrangian CCH approach to the nodal control volume and evolved the nodal control volume vertices using u_z^* . The PCH approach uses the nodal fluid velocity to evolve the control volume instead of the contact wave speed, which creates a volume change error. One way to correct this volume change error is to evolve the nodal control volumes at the contact wave speed and then remap the nodal control volume back to the location that corresponds to the PCH method. With this approach, advective fluxes are always present in the discretization including the case where the nodal velocity is equal to the fluid velocity (i.e. Lagrangian motion) so the approach is essentially Lagrangian. The volume advected is a function of the drift velocity on each interface, δu_i , which is mathematically expressed as $u_i = u_i^* - \delta u_i$. The drift velocity can be approximated by a variety of approaches. In [46], the drift velocity, δu_i , is replaced with the fastest wave speed, a , which is larger than δu_i . Using the fastest wave speed produces advective fluxes that are identical to the Rusanov dissipative fluxes. The Rusanov dissipative fluxes may advect slightly more material than required to remove the volume change error associated with the null mode. The dissipative fluxes are order h in a shock and order h^2 outside a shock; as a result, the dissipative fluxes will be equal to zero for a linear flow field and in the limit of a zero mesh size. The authors in [46] provide a more thorough discussion of this volume error and demonstrate that the Rusanov dissipative fluxes are required for convergence of the PCH approach in the Lagrangian limit – the mesh velocity is equal to the fluid velocity.

The volume change error discussed above pertains to a null mode. A null mode error differs from the volume change errors that arise from violations of the geometric conservation law (GCL) [59,71]. The GCL requires the discrete volume fluxed from the nodal control volume to be exact, and the discrete nodal control volume change that occurs from a moving mesh (e.g. Lagrange or ALE) to be exact. A numerical scheme can exactly satisfy the GCL and still have null mode errors so they are separate volume change errors. The approach in this paper will satisfy the GCL to truncation error; as a result, the GCL is identically satisfied in the limit of a zero mesh size. The first test problem in Section 8 will demonstrate convergence of the ALE PCH approach on a GCL test problem.

5. Reconstruction

The corner values are used in the multidirectional Riemann-like problem and the 1D Riemann problem. The corner values are calculated by reconstructing the variables over the nodal control volume via a linear Taylor-series expansion with a limited gradient. The approach here follows the work in [46]. The reconstruction is essential for minimizing dissipation on smooth flows. The reconstruction is

$$U_c = U_\alpha + \phi_\alpha \mathbf{x}_c \cdot \nabla U_\alpha \quad (26)$$

where U is a quantity of interest, and \mathbf{x}_c is a position vector between the node α and the tetrahedron center z . The subscript c is used because the position vector is unique to each corner, c , in the tetrahedron. The gradient above is limited by multiplying the gradient by a limiting coefficient, ϕ_α . For vector quantities, each component is projected using Eq. (26). The discrete equation for the gradient of some quantity, U , is

$$\nabla U_\alpha = \frac{1}{V_\alpha} \sum_{e \in \alpha} (\mathbf{S}_e U_e) \quad (27)$$

where the discrete surface area normal of the edge is $\mathbf{S}_e = \sum_{i \in e} (\mathbf{S}_i)$ and the surface area normal of an iota is defined in Eq. (6). The lumped volume approximation is used in this work so $V_\alpha = \frac{1}{4} \sum_{z \in \alpha} V_z$. The quantity on the edge is defined as $U_e = \frac{1}{2} (U_\alpha + U_\beta)$.

The gradient in Eq. (27) is limited by multiplying the gradient by the limiting coefficient ϕ_α that ranges between 0 and 1. A limiting coefficient of 0 eliminates the gradient and produces a 1st-order solution. The limiting process is important for creating smooth solutions around discontinuities. For a vector quantity, a limiting coefficient is found for each component. The limiting coefficient is calculated by comparing the reconstructed quantity, U , with the maximum and minimum values of this quantity at the neighboring nodes [3,60].

$$\phi_\alpha = \begin{cases} f\left(\frac{\gamma_c(U_{\max} - U_\alpha)}{U_c - U_\alpha}\right) & \text{if } U_c > U_\alpha \\ f\left(\frac{\gamma_c(U_{\min} - U_\alpha)}{U_c - U_\alpha}\right) & \text{if } U_c < U_\alpha \\ 1 & \text{if } U_c = U_\alpha \end{cases} \quad (28)$$

and the comparison function, $f(r)$, for Barth [3] approach is

$$f(r) = \min(1, r) \quad (29)$$

where r is the ratio in Eq. (28). The coefficient γ_c in the ratio reduces the maximum/minimum difference in the ratios. $\gamma_c = 0$ forces a 1st-order reconstruction in a corner and $\gamma_c = 1$ is the maximum/minimum difference in a corner which corresponds to the steepest permissible gradient. The motivation of including the coefficient γ_c is because it was shown in [45] to improve the Lagrangian mesh robustness of a calculation. In [46], the coefficient γ_c was calculated based on the deformation of the mesh, where a deformed mesh used a smaller coefficient. In this work, the coefficient is constant throughout the calculation, which follows the work in [45]. It is worth noting that a value of $\gamma_c = 0.5$ corresponds to the edge value. To see this, please consider the case where $U_\beta = U_{\max}$ and $\gamma_c = 0.5$; as a result, $\frac{1}{2}(U_\beta - U_\alpha) = \frac{1}{2}(U_\beta + U_\alpha) - U_\alpha$ where the edge value is $U_e = \frac{1}{2}(U_\beta + U_\alpha)$.

The gradient limiting process described above ensures a reconstructed corner quantity, $U_{c(\alpha)}$, for node α is bounded by the maximum and minimum neighboring nodal quantities U_β ; however, it does not guarantee that a reconstructed corner quantity is bounded by the neighboring reconstructed quantities in that corner, $U_{c(\beta)}$. As a result, a Rusanov flux (Eq. (17)) may generate negative dissipation, which is unphysical. A second limiting step is performed in every corner to ensure positive dissipation from the Rusanov flux. A corner limiting coefficient, $\phi_{c(\alpha)}$, is calculated by repeating the above gradient limiting process (Eqs. (28) and (29)) using the maximum and minimum reconstructed corner quantities in a given corner; in other words, $U_{\max} = \max_{c \in z} (U_{c(\beta)})$ and $U_{\min} = \min_{c \in z} (U_{c(\beta)})$. The corner limiting coefficient is only used in the corner where it is calculated. In summary, the process for calculating the corner values involves four steps: (1) find a single limiting coefficient, ϕ_α , for each node that ensures a bounded reconstruction, (2) use the nodal limiting coefficient and Eq. (26) to construct corner values, $\hat{U}_{c(\alpha)}$, that are bounded by the maximum/minimum neighboring nodes, (3) find a corner limiting coefficient $\phi_{c(\alpha)}$ that ensures the corner reconstructions are bounded by the other corner reconstructions, and (4) limit the reconstructed corner value using the corner limiting coefficient. The final corner quantity is given by $U_{c(\alpha)} = U_\alpha + \phi_{c(\alpha)} (\hat{U}_{c(\alpha)} - U_\alpha)$, where the hat denotes the original, limited reconstructed corner value from Eq. (26). This second limiting step improves the robustness and accuracy of the hydrodynamic approach.

6. Velocity smoothing

The mesh is smoothed by solving a Laplacian equation involving the mesh velocity, that was developed by Waltz et al. [67]. The mesh smoothing equation is

$$\nabla^2 \mathbf{w}_\alpha = 0. \quad (30)$$

The Laplacian is solved to a specified tolerance, ϵ , using a preconditioned conjugate gradient method. The initial mesh velocity in the Laplacian is a function of the current fluid velocity,

$$\mathbf{w}_\alpha = \mu_\alpha \mathbf{u}_\alpha. \quad (31)$$

Each component of the initial mesh velocity is equal to the fluid velocity multiplied by a smoothing coefficient. The smoothing coefficient on each vector component is defined as,

$$\mu_\alpha = c_1 \max\left(0, 1 - c_2 \frac{\|\boldsymbol{\omega}_\alpha\|}{\|\boldsymbol{\omega}_p\|_\infty}\right) \quad (32)$$

where $\boldsymbol{\omega}$ is the vorticity vector, and the coefficients c_1 and c_2 are user-defined. The three velocity components use the same c_2 coefficient; however, the coefficient c_1 is allowed to be defined differently for each velocity component. If the smoothing coefficients are all equal to zero, then the mesh will be stationary, which corresponds to the Eulerian solution. A benefit of this definition is the smoothing approach can increase the amount smoothing in regions of higher vorticity or bias the smoothing in a particular, user-defined direction.

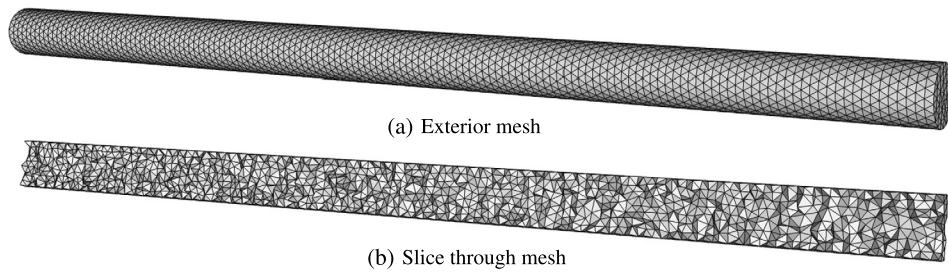


Fig. 4. An unstructured tetrahedral mesh was used for the GCL problem. The average mesh resolutions used are: 0.840 cm, 0.414 cm, 0.206 cm, and 0.103 cm respectively. The exterior mesh and a slice through the center of the mesh are shown above corresponding to an average resolution of 0.840 cm.

7. Computational procedure

The algorithm presented in this paper is collocated in time and space. The solution details that follow are for one temporal integration step in the Runge–Kutta integration method such as evolving the solution from time level n to $n + 1/2$.

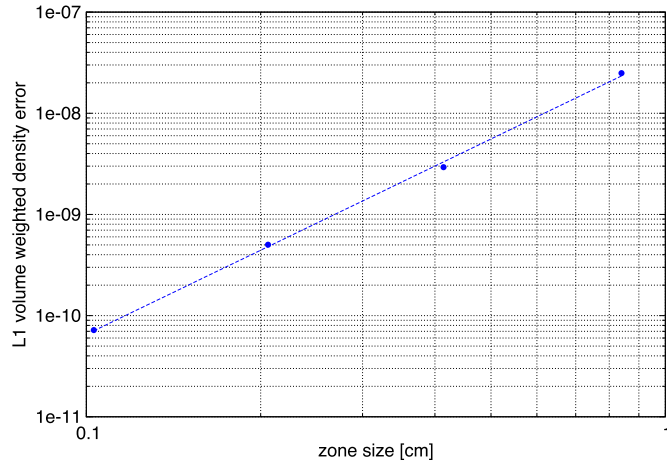
- The first step in the solution process is to calculate a nodal mesh velocity by smoothing the velocity field at the current time level (Eq. (30)). This first step is not needed with the Eulerian and Lagrangian calculations because the mesh velocity is known. For an Eulerian calculation, the mesh velocity is 0, and for a Lagrangian calculation, the mesh velocity is equal to the fluid velocity.
- The second step is to calculate the nodal gradients (Eq. (27)) for the density, velocity, internal energy, and pressure. These nodal gradients are used to reconstruct the fields (e.g. velocity field) over the nodal control volume.
- The third step is to project the variables (Eq. (26)) to the corners of the nodal control volume, which correspond to the center of a tetrahedron. The reconstructed corner values are then limited so that the solution is smooth around discontinuities (Eq. (28)). These limited corner values will be used to calculate the advective fluxes and the dissipative fluxes; in addition, the limited corner values will be used in the multidirectional Riemann like problem. The follow steps describe this in further detail.
- The fourth step is calculate an estimate for the shock velocity, $a = c + b_1 \delta u$, using the corner values. The shock velocity is used in the Riemann problems.
- The fifth step is to calculate the Riemann velocity at the center of each tetrahedron by solving the multidirectional approximate Riemann problem (Eq. (15)).
- The sixth step is to use the Riemann velocity at the center of the tetrahedron and calculate the Riemann force on each iota surface (Eq. (16)).
- The seventh step is to calculate the advective and dissipative face fluxes, which involves solving a 1D Riemann problem (Eq. (17)) on each iota surface at the tetrahedron center. The solution to the 1D approximate Riemann problem is the average of the two corner values on the iota surface, Eq. (19). The fluxed volume in the advective flux is a function of the difference between the mesh velocity and the fluid velocity at the tetrahedron edge, $\mathbf{S}_i \cdot (\mathbf{w}_e - \mathbf{u}_e)$.
- All terms in the fluxes shown in Eq. (7) are known. These fluxes govern how the unknowns change with time (Eq. (4)) so the next step is to evolve the solution forward temporally (Eq. (8) or Eq. (10)). The mesh is also evolved temporally forward in time using the mesh velocity (Eq. (9) or Eq. (11)).
- The new volume of the nodal control volume is calculated using the new mesh locations.
- The solution process ends with calculating the new density, velocity, specific total energy, and specific internal energy at the node.

The process described above is repeated for every Runge–Kutta step.

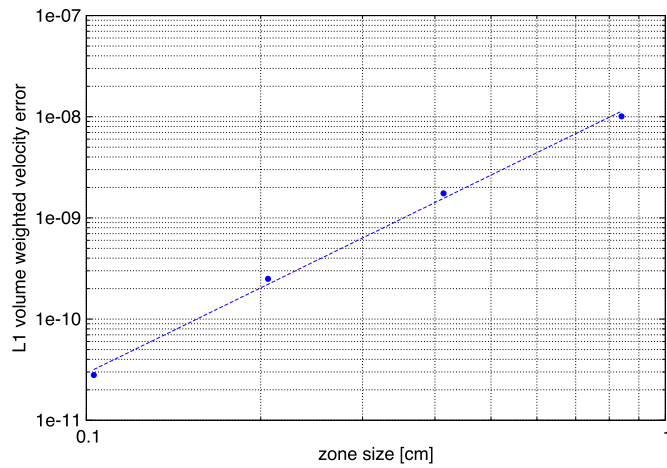
8. Test problems

A series of tests were performed to assess the accuracy and robustness of the new PCH approach. The tests are as follows:

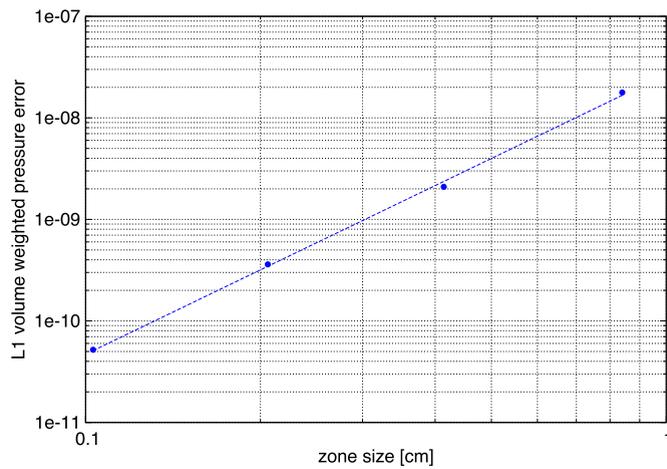
- Geometric conservation law (GCL) [59,71]
- Sod [57]
- Sedov XY [55]
- Sedov XYZ [55]
- Saltzman [42,21,5]
- Kidder shell [31,30,32,50]
- Kidder sphere [12,50]
- Taylor Green
- Triple-point [34]



(a) Density Error



(b) Velocity Error



(c) Pressure Error

Fig. 5. Convergence plots are shown for density, velocity, and pressure fields for the GCL problem. The density errors are converging to zero at a rate of 2.7 and the power-law fit has an R^2 of 0.9994. The velocity errors are converging to zero at a rate of 2.8 and the power-law fit has an R^2 of 0.9985. The pressure errors are converging to zero at a rate of 2.8 and the power-law fit has an R^2 of 0.9994.

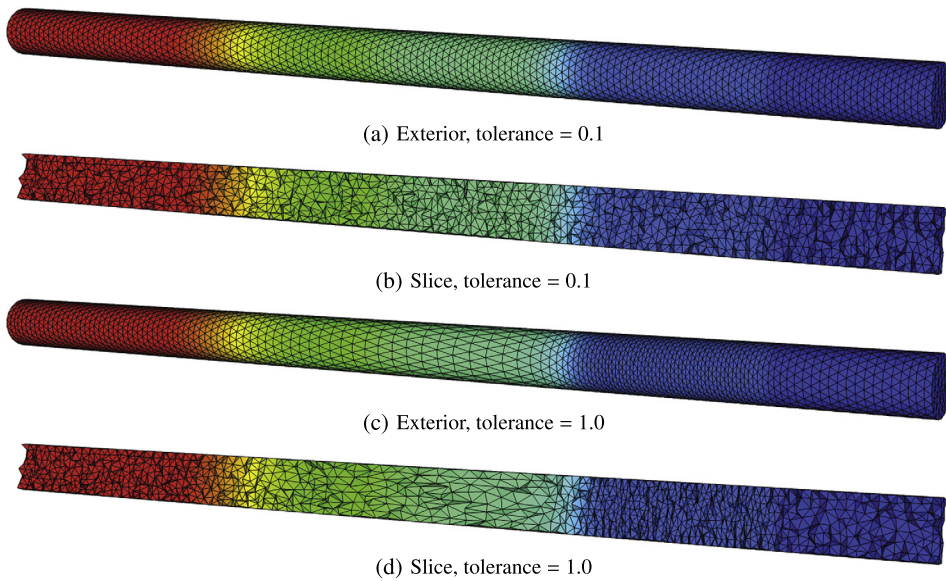


Fig. 6. The ALE results are shown at $t = 20 \mu\text{s}$ using two values for the mesh velocity smoothing tolerance – 0.1 and 1.0 respectively. The average mesh resolution at the start of the calculation is 0.840 cm. The exterior mesh and a slice through the center of the mesh are provided. A small tolerance will smooth the mesh velocity more than a larger tolerance. The ALE scatter plots are provided in the following two figures.

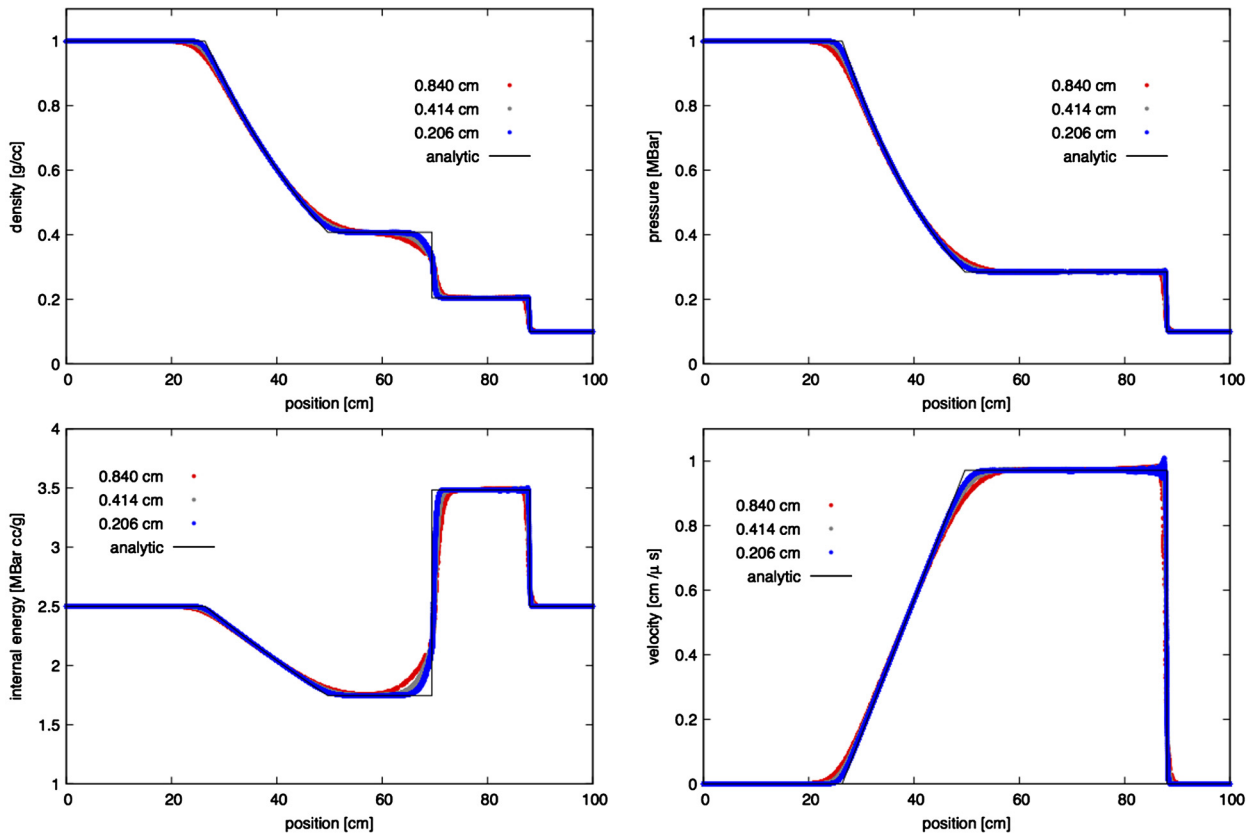


Fig. 7. The scatter plots for the Sod problem are shown using the ALE approach with a mesh velocity smoothing tolerance of 0.1. The results are at $t = 20 \mu\text{s}$. Every nodal value in the mesh is plotted.

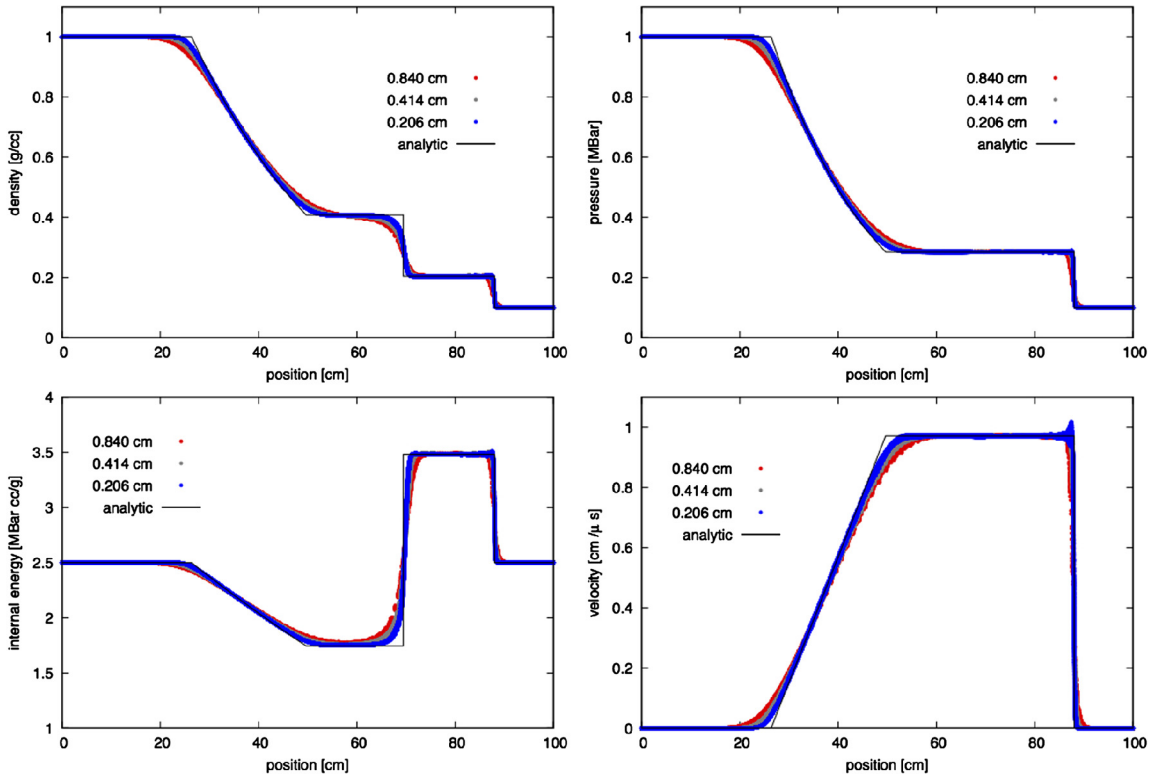


Fig. 8. The scatter plots for the Sod problem are shown using the ALE approach with a mesh velocity smoothing tolerance of 1.0. The results are at $t = 20 \mu\text{s}$. Every nodal value in the mesh is plotted.

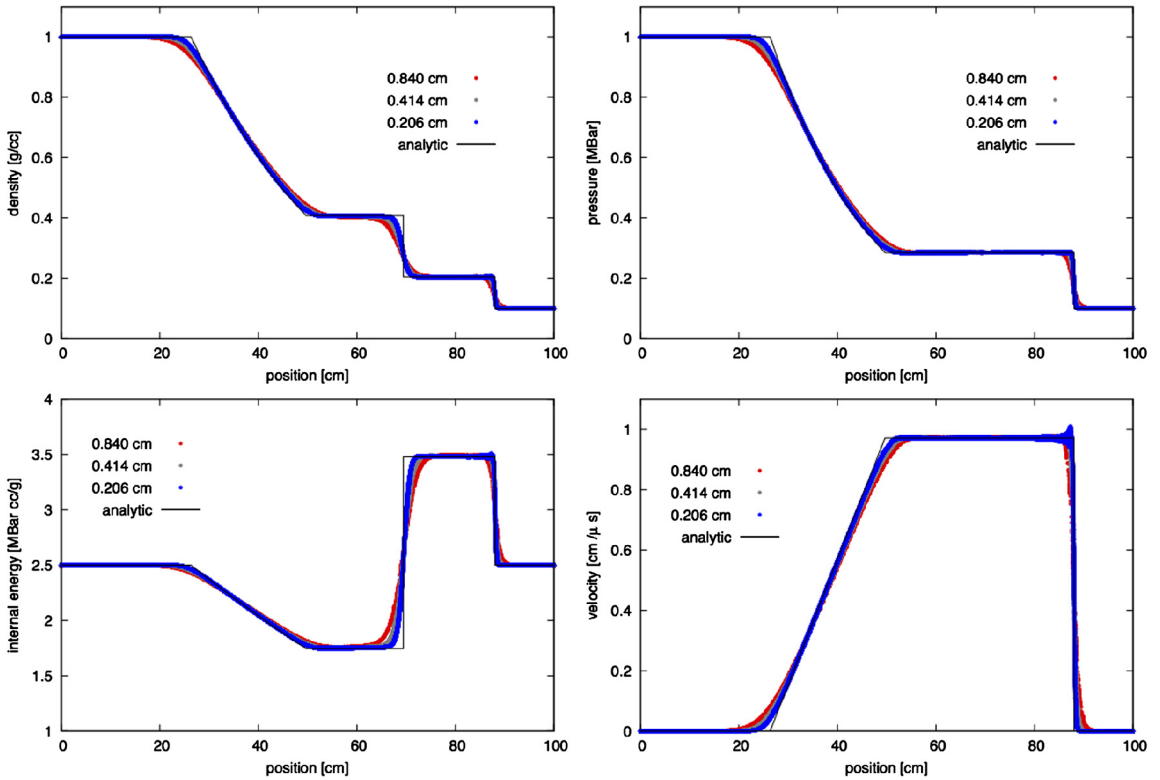


Fig. 9. The scatter plots for the Sod problem are shown using the Eulerian approach. The results are at $t = 20 \mu\text{s}$. Every nodal value in the mesh is plotted.

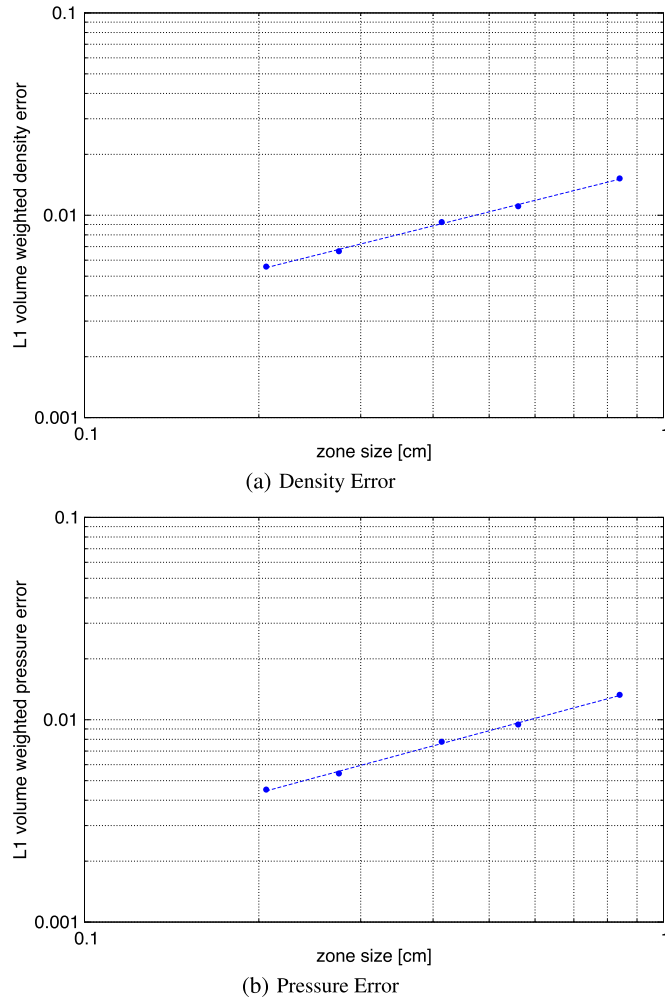


Fig. 10. Convergence plots are shown for the density and the pressure fields for the Sod problem using unstructured tetrahedral meshes and the ALE approach with a tolerance of 0.1. The density errors are converging to zero at a rate of 0.72 and the power-law fit has an R^2 of 0.9989. The pressure errors are converging to zero at a rate of 0.77 and the power-law fit has an R^2 of 0.9989.

These test problems were chosen because they are commonly used in other ALE research efforts [67,5,4]. Each test problem will be discussed in detail.

8.1. Error metrics

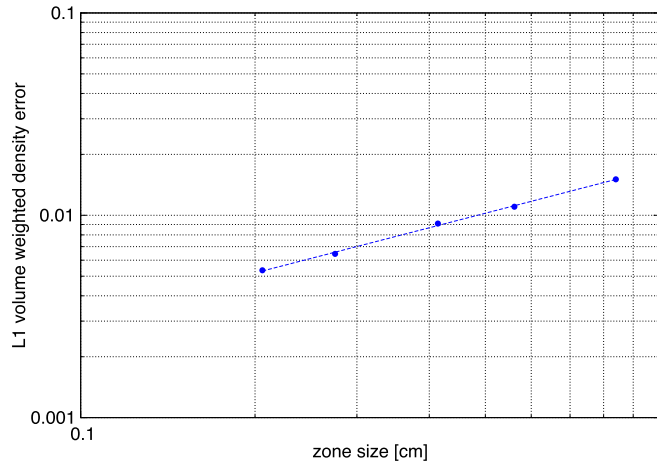
Error metrics will be used to quantify numerical errors and to demonstrate convergence toward the analytic solution as the mesh is refined. The convergence is calculated using an L1 error norm that is weighted by the volume [19]. The L1 error norm for an unknown, U , is calculated using

$$L_U^1 = \frac{\sum_{p \in \mathcal{R}} (V_p |U_p - U_{exact}|)}{\sum_{p \in \mathcal{R}} V_p} \quad (33)$$

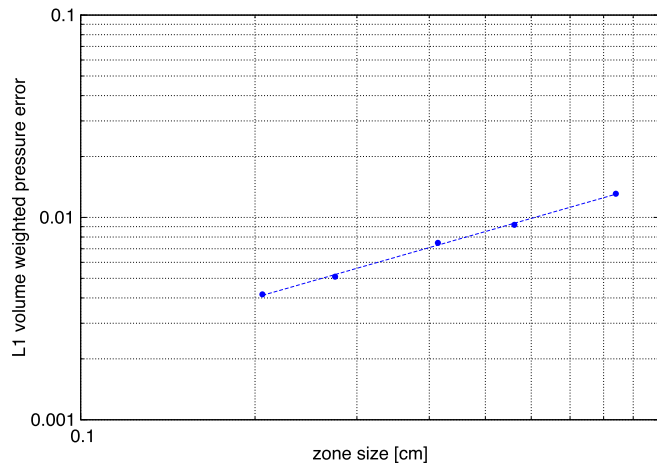
where the domain of the problem is denoted with \mathcal{R} . This error norm is used for every convergence study in this paper.

8.2. GCL

To satisfy the geometric conservation law (GCL) [59,71], the algorithm must exactly capture the change in the volume of the control volume. In other words, the GCL requires the volume fluxed from the nodal control volume to be exact, and the nodal control volume change that occurs from a moving mesh (e.g. Lagrange or ALE) to be exact. The PCH ALE algorithm presented in this paper will satisfy GCL to truncation error so the PCH ALE algorithm will satisfy the GCL in the



(a) Density Error



(b) Pressure Error

Fig. 11. Convergence plots are shown for the density and the pressure fields for the Sod problem using unstructured tetrahedral meshes and the Eulerian approach. The density errors are converging to zero at a rate of 0.74 and the power-law fit has an R^2 of 0.9991. The pressure errors are converging to zero at a rate of 0.82 and the power-law fit has an R^2 of 0.9989.

limit of a zero mesh size. A test problem will be performed to quantify the volume errors associated with the GCL. The GCL test problem involves moving the mesh at an arbitrary velocity with uniform pressure, density, internal energy, and velocity fields. For a uniform density field, the volume change equation is identical to the conservation of mass equation (Eq. (1)).

$$\rho \left(\frac{d}{dt} \int_V dV + \oint_{\partial V} (d\mathbf{S} \cdot (\mathbf{u} - \mathbf{w})) \right) = 0 \quad \text{for } \rho = \text{constant} \quad (34)$$

where the term inside the brackets is the volume evolution equation for a moving mesh. The density field should remain constant in time; however, volume errors will perturb the density field. The sources of volume errors in this PCH ALE approach are the lumped volume approximation ($V_p = \frac{1}{4} \sum_{z \in p} V_z$) and the volume fluxed through the nodal control volume surface. The mesh velocity used in the GCL test problem is

$$\mathbf{w}_p = \sin^2 \left(\frac{\pi x}{L} \right) \quad (35)$$

where L is the domain length. The problem is calculated for 10 cycles.

In this work, The GCL problem is calculated on a tube that is discretized with an unstructured tetrahedral mesh (Fig. 4). The tube meshes have an exterior diameter of 5 cm and a length of 100 cm. The average mesh resolutions are 0.840 cm, 0.414 cm, 0.206 cm, and 0.103 cm respectively. These tube meshes are identical to those used to model the GCL test problem in [67], which facilitates comparisons between the two approaches. The convergence results are plotted in Fig. 5. The errors

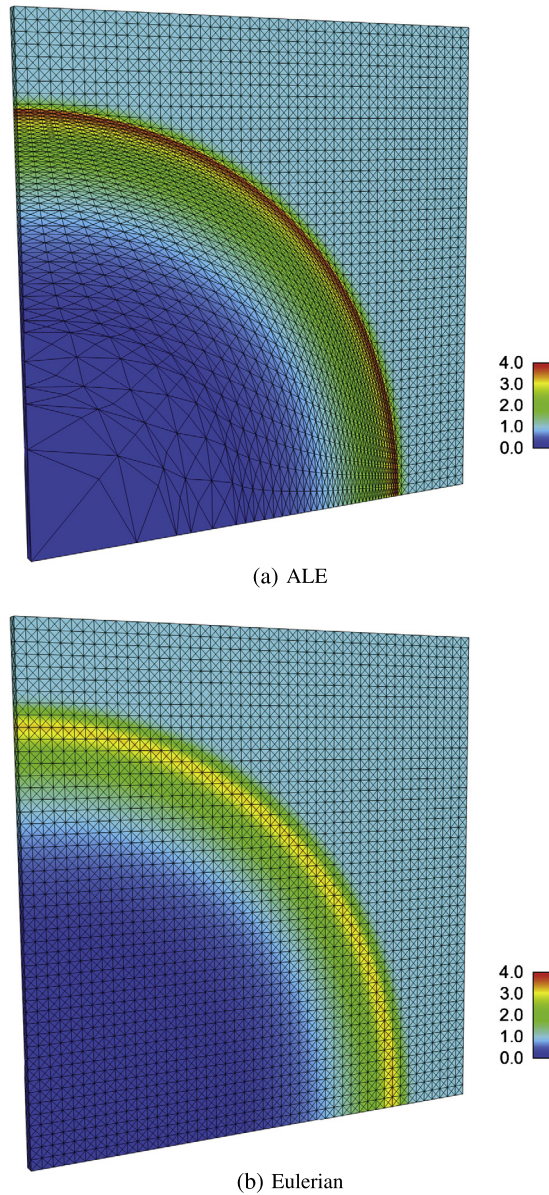


Fig. 12. The density field for the Sedov 2D Cartesian problem is shown using the $48 \times 48 \times 2$ mesh. The ALE result is shown on the top and the Eulerian result is shown on the bottom. The results are at $1 \mu\text{s}$. The corresponding scatter plots are provided in Fig. 13. (For interpretation of the colors in this figure, the reader is referred to the web version of this article.)

in the density, pressure, and velocity that are created by volume errors are very small and are converging toward zero at a rate of about 2.8.

8.3. Sod

The Sod problem [57] is a 1D shock problem in a gamma-law gas. The shock is generated by a contact discontinuity. The gamma used in this study is 1.4. The initial conditions are as follows. The initial velocity is equal to zero and the initial internal energy is equal to 2.5 over the entire domain. The initial density and pressure are given by

$$\rho = p = \begin{cases} 1.0, & x < 50 \\ 0.1, & x \geq 50. \end{cases} \quad (36)$$

The Sod problem is calculated in the ALE and Eulerian reference frames. The essentially Lagrangian results are provided in [46]. The meshes used for this test problem are identical to the meshes that were used with the GCL test problem. In addition, these tube meshes are identical to those used to model the Sod problem in [67,68], which facilitates comparisons

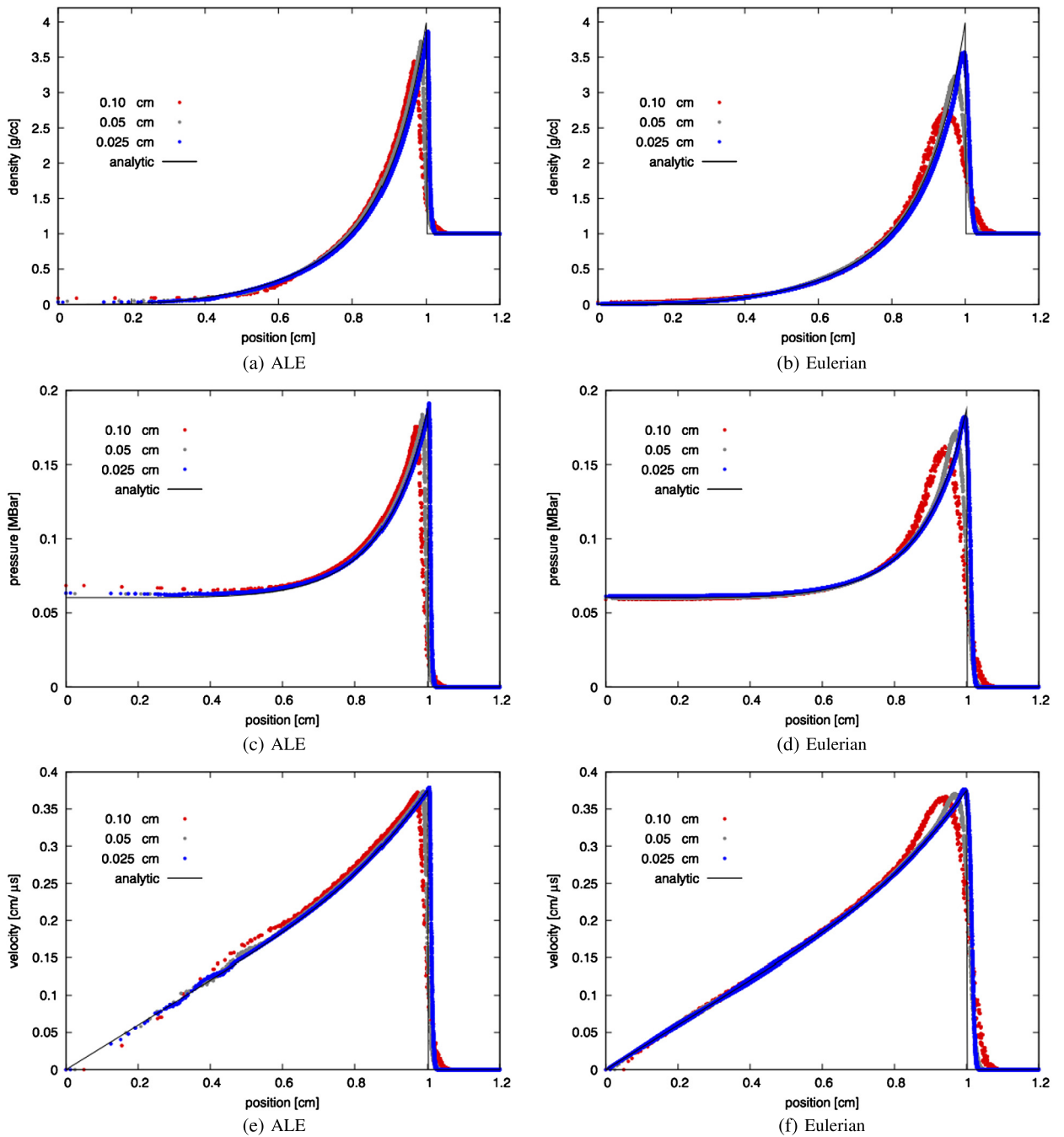


Fig. 13. The scatter plots for the Sedov 2D Cartesian problem are shown using the ALE (left column) and Eulerian (right column) approaches. The results are at 1 μs. Every nodal value in the mesh is plotted.

between the different methods. The average mesh resolutions used are: 0.840 cm, 0.414 cm, and 0.206 cm respectively. For the ALE calculations, the mesh velocity smoothing parameters are $c_1 = 1.0$ and $c_2 = 0.0$. On this test problem, we tested two different tolerances for solving the Laplacian (Eq. (30)). The first tolerance is 0.1 and the second tolerance is 1.0. A small tolerance will produce a solution closer to the Eulerian limit, and a larger tolerance generates a solution that is closer to the Lagrangian limit. The goal of using different tolerance values is to illustrate the ALE approach produces accurate solutions over a range of settings ranging from nearly Lagrangian to the Eulerian limit.

Fig. 6 shows the final meshes for both ALE test cases. The ALE scatter plots are presented in Fig. 7 for a tolerance of 0.1, and Fig. 8 shows the results for a tolerance of 1.0. The Eulerian scatter plots are shown in Fig. 9. As shown in the scatter plots, there is very little scatter in the results and the solution is in good agreement with the analytic solution. Every nodal

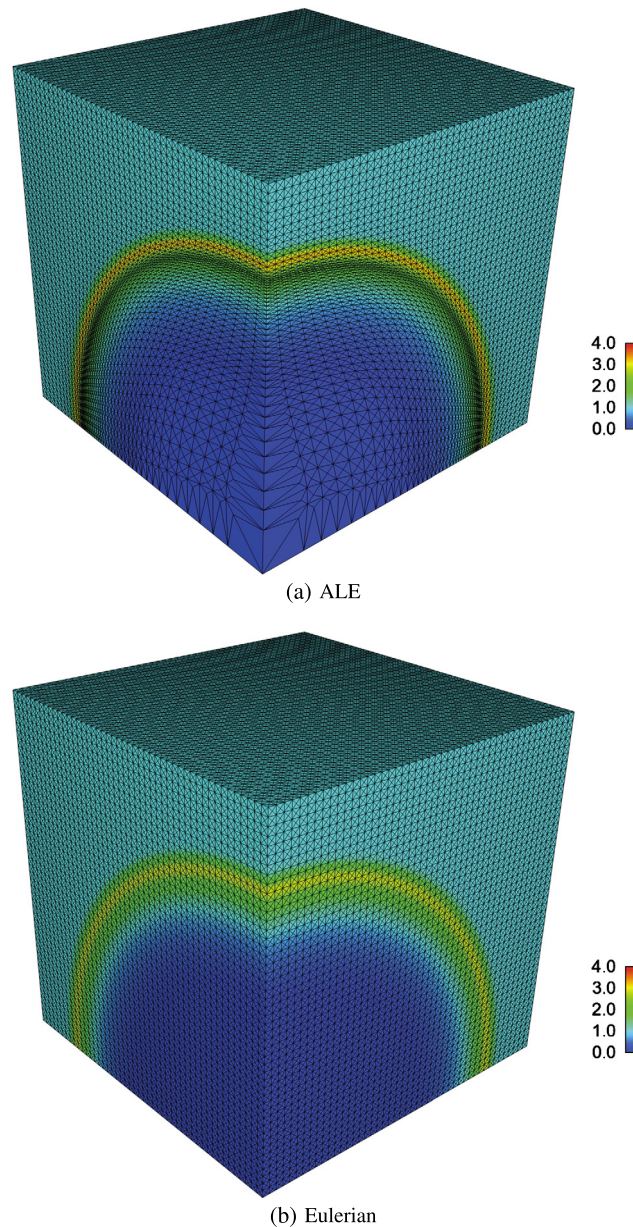


Fig. 14. The density field for the Sedov 3D Cartesian problem is shown using the $48 \times 48 \times 48$ mesh. The ALE result is shown on the top and the Eulerian result is shown on the bottom. The results are at $1 \mu\text{s}$. The corresponding scatter plots are provided in Fig. 15. (For interpretation of the colors in this figure, the reader is referred to the web version of this article.)

value in the mesh is plotted in the scatter plots. The convergence rate of the density errors with the ALE approach using a tolerance of 0.1 is 0.72 and the convergence rate of the pressure errors is 0.77 (see Fig. 10). The convergence rate of the density errors with the Eulerian approach is 0.74 and the convergence rate of the pressure errors is 0.82 (see Fig. 11). These convergence rates are consistent with Lagrangian PCH, SGH and CCH methods on the Sod test problem [46,22].

8.4. Sedov

The Sedov problem [55] is an outward traveling blast wave in a gamma-law gas that is initiated by an energy source. The Sedov problem is calculated in both XY and XYZ coordinates. The gamma used in this study is $5/3$ and the initial density is 1 g/cc . The source energies are chosen so that the shock is located at 1 cm at $1 \mu\text{s}$. The extensive source internal energy is 0.564113 (XY) or 0.493390 (XYZ). For the XY problem, the source energy is applied to the nodes along the z-axis because the mesh is a thin slab. Results are obtained in the ALE and Eulerian reference frames. The essentially Lagrangian results are provided in [46]. The first set of meshes were created by decomposing a hexahedral mesh into 24 tetrahedra per

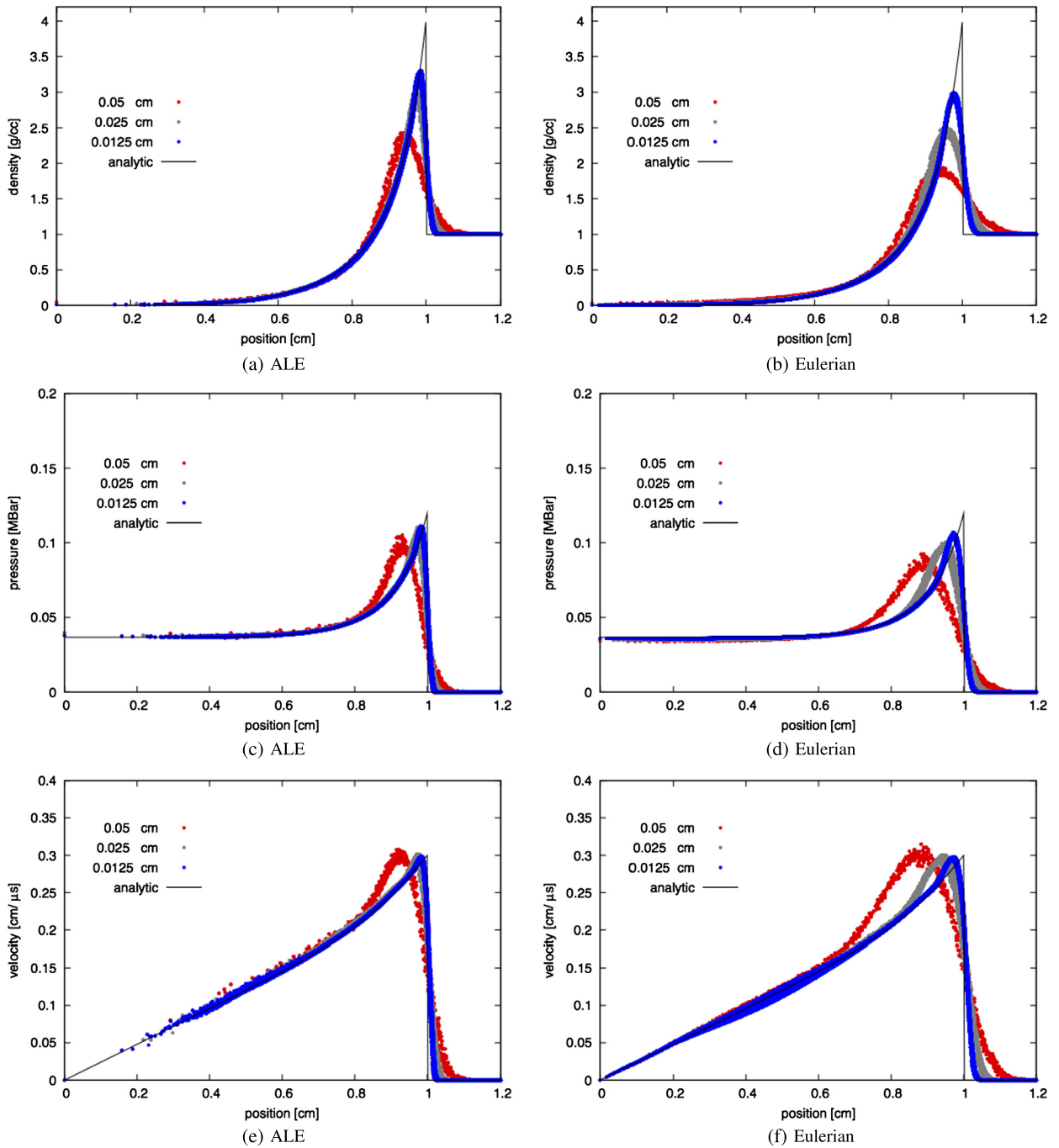


Fig. 15. The scatter plots for the Sedov 3D Cartesian problem are shown using the ALE (left column) and Eulerian (right column) approaches. The results are at 1 μs. Every nodal value in the mesh is plotted.

hexahedron, which follows Lagrangian works in [53,46,68]. The XY domain is 1.2 cm × 1.2 cm and the hexahedral mesh resolutions are 24 × 24 × 2, 48 × 48 × 2, and 96 × 96 × 2. The depth of the XY mesh is chosen to make uniform cells. Next, the XYZ domain is 1.2 cm × 1.2 cm × 1.2 cm and the hexahedral meshes are 12 × 12 × 12, 24 × 24 × 24, and 48 × 48 × 48. For the Sedov XYZ problem, calculations were also performed on a highly unstructured tetrahedral mesh with the ALE and the Eulerian approaches. The goal of the unstructured meshes is to quantify symmetry errors that can arise on highly unstructured meshes. For the ALE calculations, the mesh velocity smoothing parameters are $c_1 = 1.0$ and $c_2 = 0.0$; likewise, the Laplacian (Eq. (30)) is solved until a tolerance of 0.1 is reached.

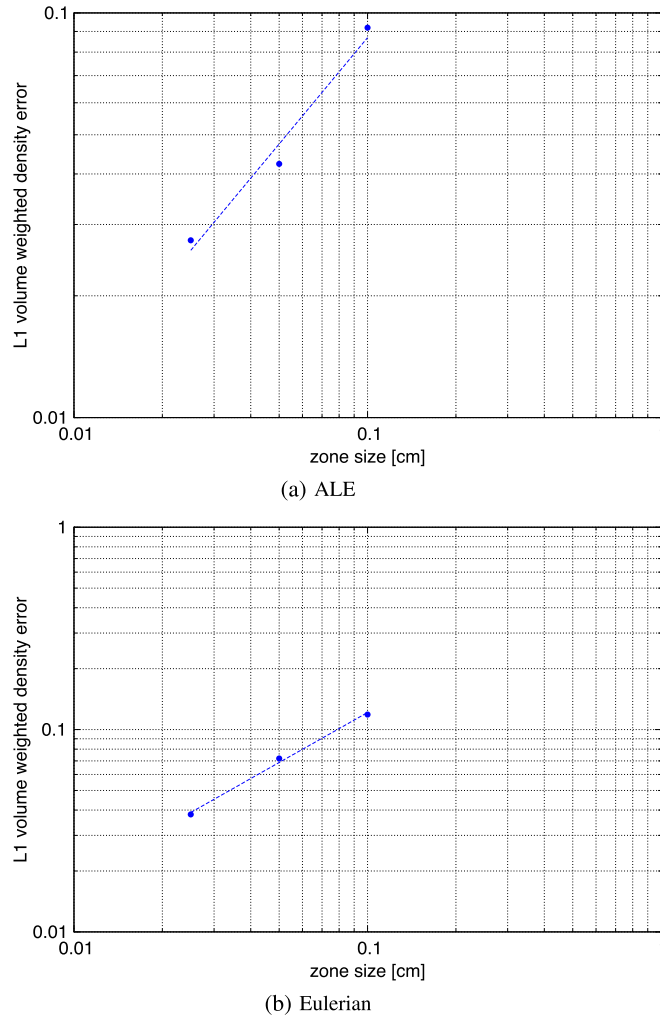


Fig. 16. Density convergence plots are shown for the Sedov 3D Cartesian problem using the ALE and Eulerian approaches. The density errors with the ALE approach are converging to zero at a rate of 0.87 and the power-law fit has an R^2 of 0.9871. Next, the density errors with the Eulerian approach are converging to zero at a rate of 0.82 and the power-law fit has an R^2 of 0.9975.

The Sedov XY results are shown in Figs. 12 and 13. Every nodal value in the mesh is plotted in the scatter plots. As shown in these figures, the mesh is smooth and the calculations are in good agreement with the analytic solution. Likewise, the calculations are very symmetric. The Sedov XYZ results are shown in Figs. 14 and 15. The density convergence results for Sedov XYZ are shown in Fig. 16. The density errors with the ALE approach are converging toward zero at a rate of 0.87 and with the Eulerian approach the errors are converging toward zero at a rate of 0.87. The Sedov XYZ results for the unstructured tetrahedral mesh are shown in Figs. 17 and 18. As demonstrated in the Sedov XYZ calculations, the mesh quality is excellent and the solution is in good agreement with the analytic solution. The solutions are also very symmetric.

8.5. Saltzman

The Saltzman problem is commonly used to test the robustness of a Lagrangian method [53,45,46]. In this paper, we follow [5] and use this test problem to assess the robustness of the ALE approach. The Saltzman problem is a piston driven shock through an initially skewed mesh. The skewed tetrahedral mesh is built by decomposing a skewed hexahedron into 24 tetrahedral zones per hexahedron [53]. The nodal coordinates of the skewed hexahedral mesh are given by

$$\begin{aligned}
 x_p &= (i - 1.0) \Delta x + (N_y - j) \Delta y \sin\left(\pi \frac{i - 1}{N_x - 1}\right) \\
 y_p &= (j - 1.0) \Delta y \\
 z_p &= (k - 1.0) \Delta z
 \end{aligned}
 \tag{37}$$

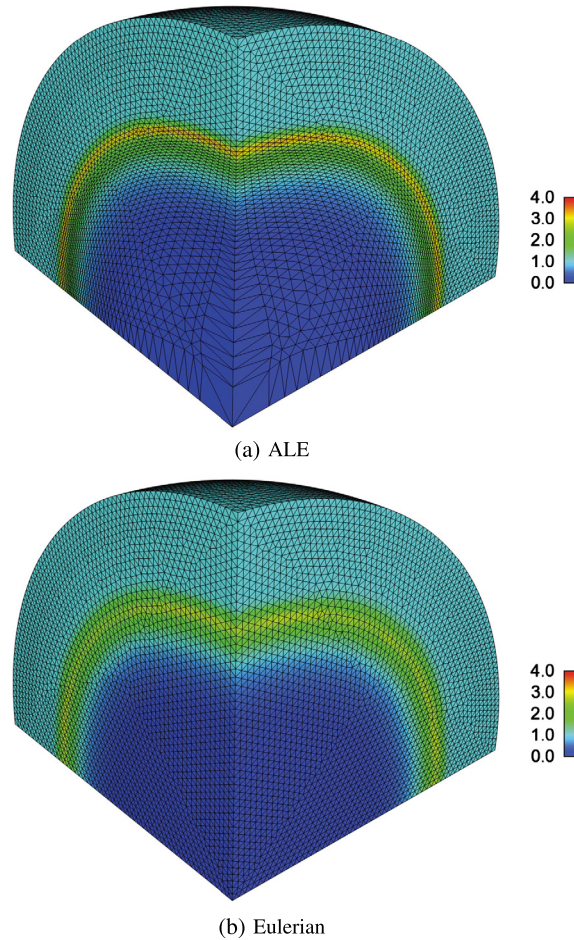


Fig. 17. The density field for the Sedov 3D Cartesian problem is shown using a highly unstructured tetrahedral mesh. The nominal mesh resolution is 0.024 cm. The ALE result is shown on the top and the Eulerian result is shown on the bottom. The results are at $1 \mu\text{s}$. The corresponding scatter plots are provided in Fig. 18. (For interpretation of the colors in this figure, the reader is referred to the web version of this article.)

where i , j , and k are integers in the following ranges: $i \in [1 : N_x]$, $j \in [1 : N_y]$, and $k \in [1 : N_z]$. The number of mesh points in the respective directions are N_x , N_y , and N_z . The uniform mesh resolutions are Δx , Δy , and Δz . The length of the shock tube is 1 cm, and the width and the height of the shock tube were chosen to make square hexahedral zones if the mesh were not skewed. The standard Saltzman problem uses 100×10 nodes and a quadrilateral mesh. The 3D tetrahedral mesh is constructed from a hexahedral mesh with $100 \times 10 \times 10$ nodes. The initial tetrahedral mesh is shown in Fig. 19. This problem is calculated using the ALE approach and the mesh velocity smoothing settings are $\mathbf{c}_1 = [1.0, 0.0, 0.0]$ and $c_2 = 0.0$. The Laplacian (Eq. (30)) is solved until a tolerance of 0.1 is reached.

The mesh at $0.7 \mu\text{s}$ and $0.8 \mu\text{s}$ is shown in Fig. 20. The scatter plots for density, pressure, and specific internal energy at $0.7 \mu\text{s}$ and $0.8 \mu\text{s}$ are shown in Fig. 21. Every nodal value in the mesh is plotted in the scatter plots. A time of $0.7 \mu\text{s}$ was chosen so that comparison can be made to the published ALE results in [5] and the Lagrangian results in [53,46]. Likewise, we include ALE results at $0.8 \mu\text{s}$ to demonstrate the robustness and accuracy of the approach after the shock reflects from the wall. As demonstrated, the ALE approach performs well on this test problem.

8.6. Kidder shell

Kidder [31,30,32,50] derived a series of exact solutions for the isentropic compression of a gas. In this subsection, we calculate the isentropic compression of a hollow shell of gas [32]. This test problem is calculated in other hydrodynamic papers including [5,10,61]. Time-varying boundary conditions on the inner and outer surfaces cause the shell to compress. The goal of the Kidder hollow shell test problem is to quantify dissipation errors and assess the ability of the algorithm to produce symmetric results. The test problem is isentropic, so zero dissipation should be generated. The equation of state is a gamma law gas with gamma equal to $5/3$. The initial conditions of this test problem are as follows. The initial inner and outer radii of the shell are $r_1^0 = 0.9$ cm and $r_2^0 = 1.0$ cm respectively. The subscripts 1 and 2 denote the inner and outer

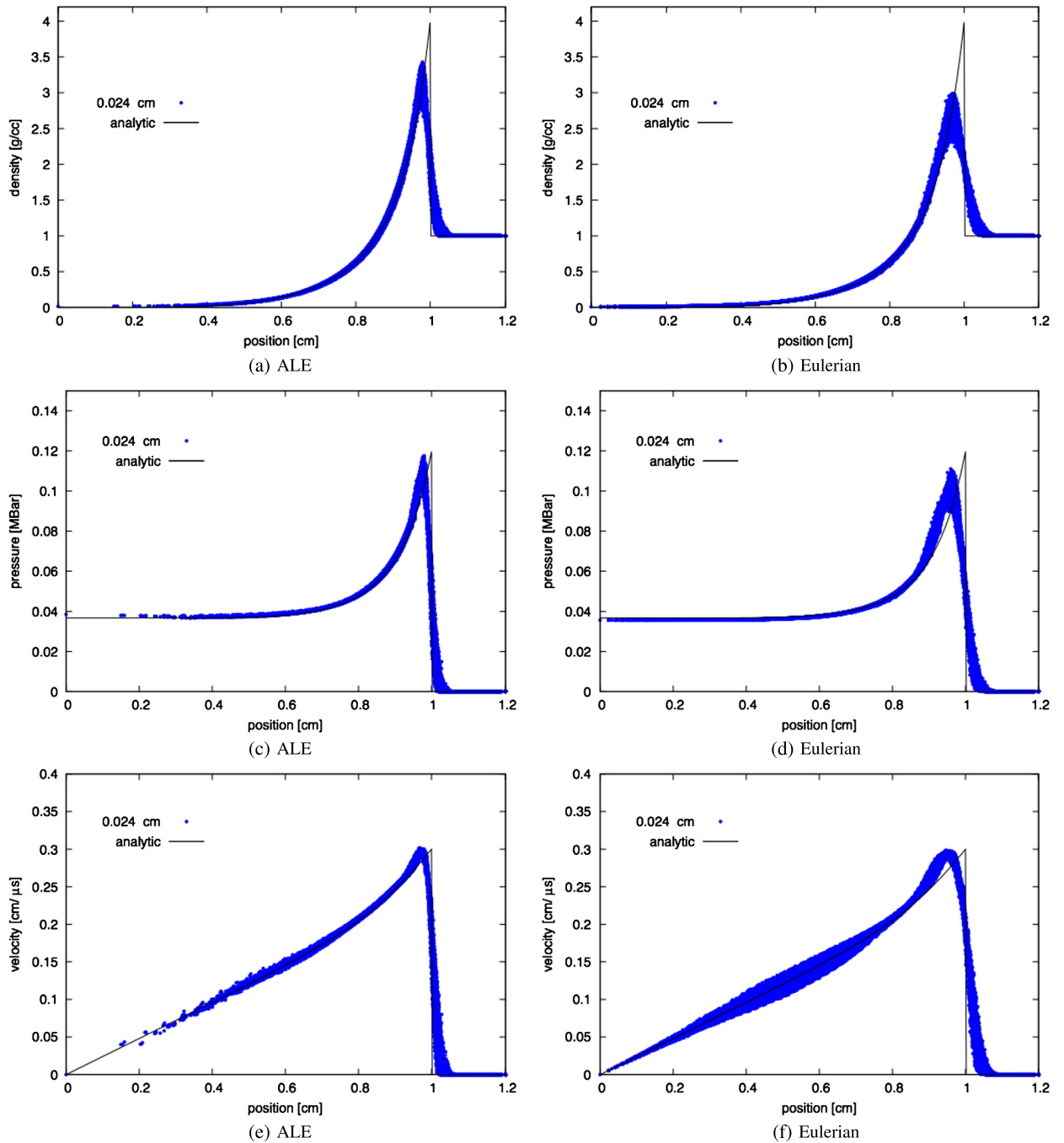


Fig. 18. The scatter plots for the Sedov 3D Cartesian problem using a highly unstructured tetrahedral mesh are shown. The ALE results are shown in the left column and Eulerian results are shown in the right column. The results are at 1 μ s. Every nodal value in the mesh is plotted.

surfaces and the superscript 0 denotes the initial time. The initial density on the inner and outer surfaces are $\rho_1^0 = 1$ g/cc and $\rho_2^0 = 2$ g/cc. The initial density, pressure, and velocity distributions in the shell are given by

$$\rho^0(r) = \left(\frac{r_2^2 - r^2}{r_2^2 - r_1^2} \rho_1^{\gamma-1} + \frac{r^2 - r_1^2}{r_2^2 - r_1^2} \rho_2^{\gamma-1} \right)^{\frac{1}{\gamma-1}}$$

$$p^0(r) = \rho^0(r)^\gamma$$

$$u^0(r) = 0$$

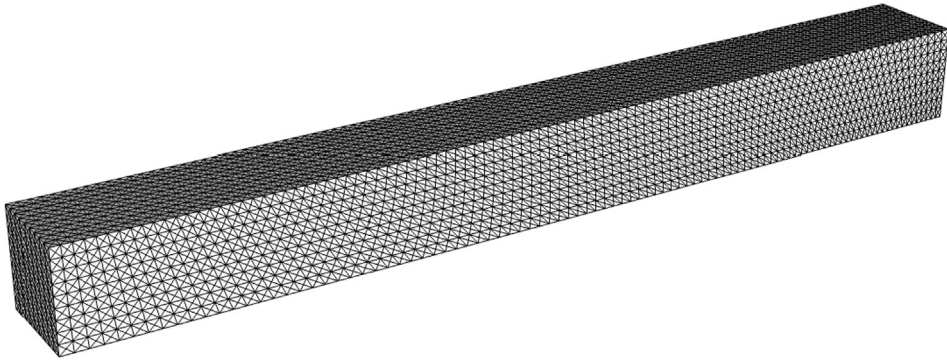


Fig. 19. The initial mesh used with the Saltzman problem is shown. This test problem is calculated using the ALE approach.

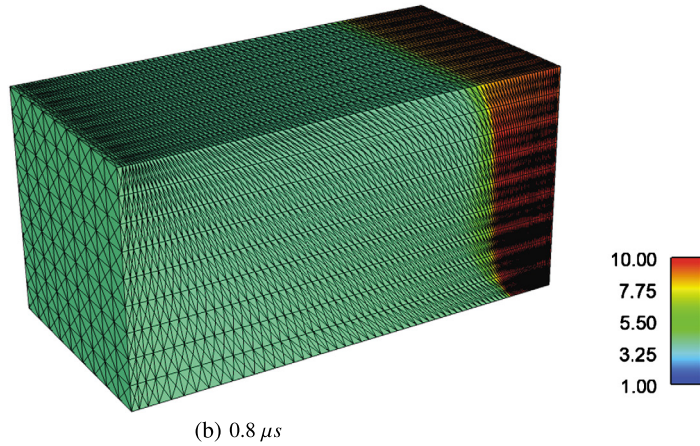
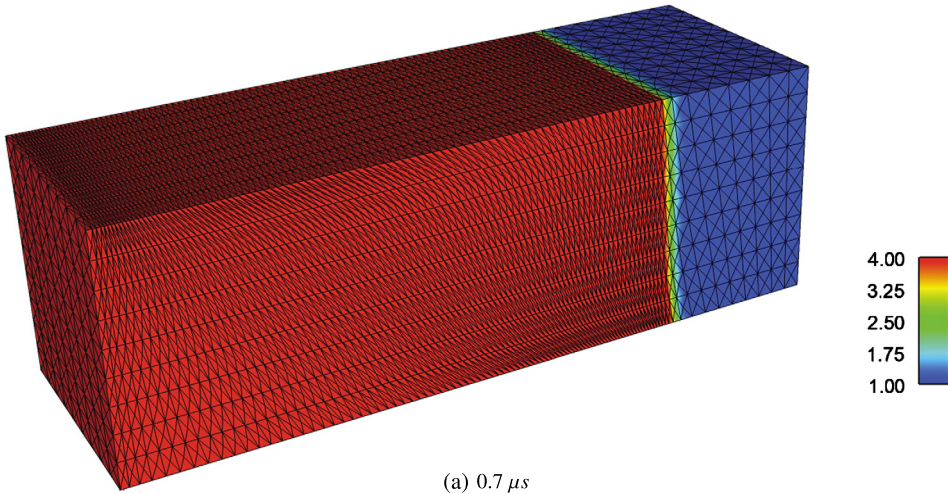


Fig. 20. The mesh and density in the Saltzman problem are shown at 0.7 μs and at 0.8 μs . The density scale varies between the two images to elucidate the details of the flow. The scatter plots for density, pressure, and specific internal energy are provided in Fig. 21. The initial mesh is shown in Fig. 19. (For interpretation of the colors in this figure, the reader is referred to the web version of this article.)

where the radius is $r = \sqrt{x^2 + y^2 + z^2}$. The analytic solution for the density, pressure, and velocity as a function of the radius and time are

$$\begin{aligned}
 \rho(r(t), t) &= \rho^0(r^0)h(t)^{\frac{-2}{\gamma-1}} \\
 p(r(t), t) &= p^0(r^0)h(t)^{\frac{-2\gamma}{\gamma-1}} \\
 u(r(t), t) &= r^0 \frac{dh(t)}{dt}
 \end{aligned}
 \tag{39}$$

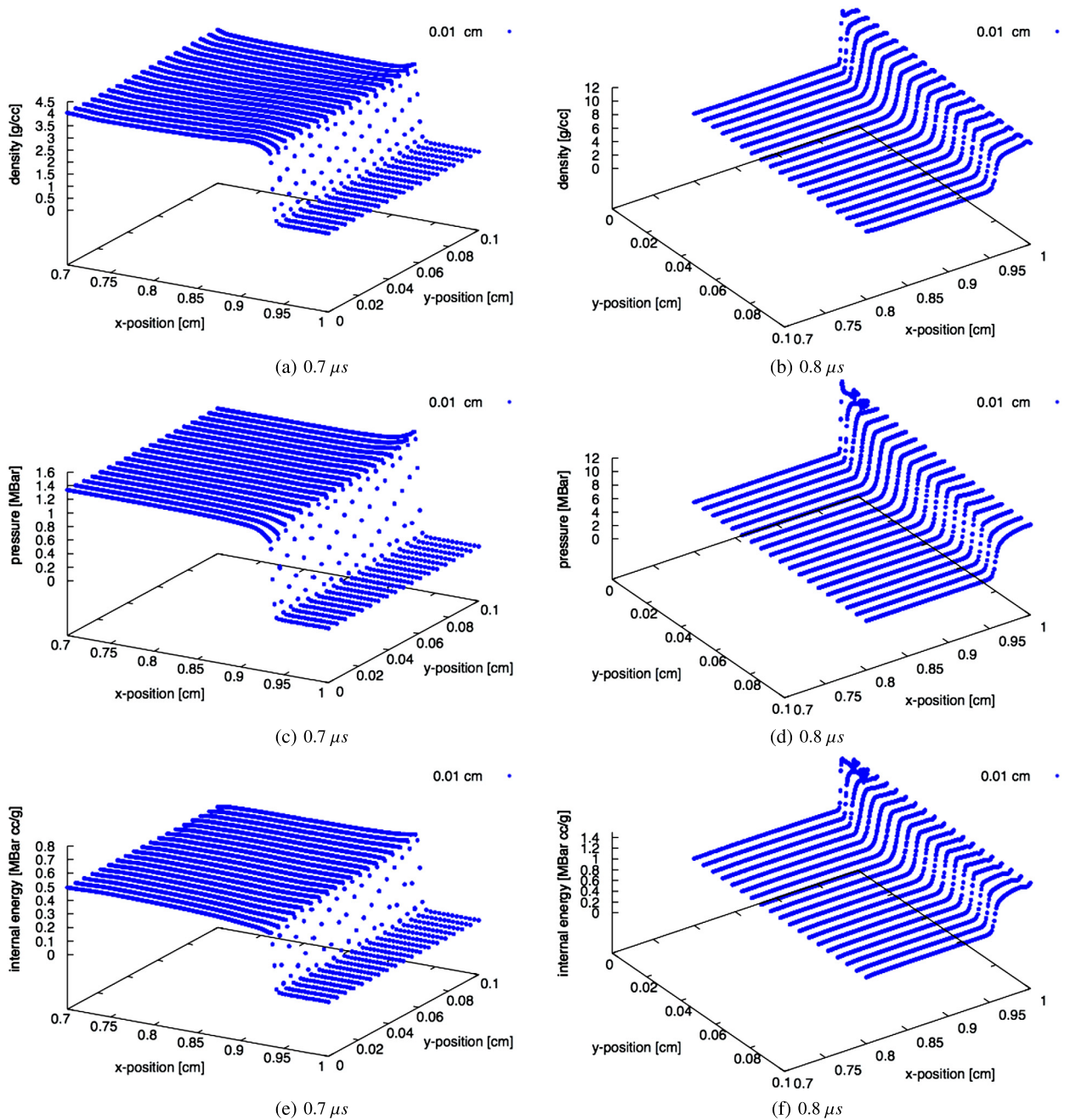


Fig. 21. The scatter plots for the Saltzman problem at $0.7 \mu s$ (left side) and $0.8 \mu s$ (right side) are shown.

The radius varies with time according to

$$r(t) = r^0 h(t) \tag{40}$$

The analytic solutions in Eq. (39) and the radius are functions of the initial radius r^0 and a non-dimensional variable $h(t)$. The variable $h(t)$ is given by

$$h(t) = \sqrt{1 - \frac{t^2}{\tau^2}} \tag{41}$$

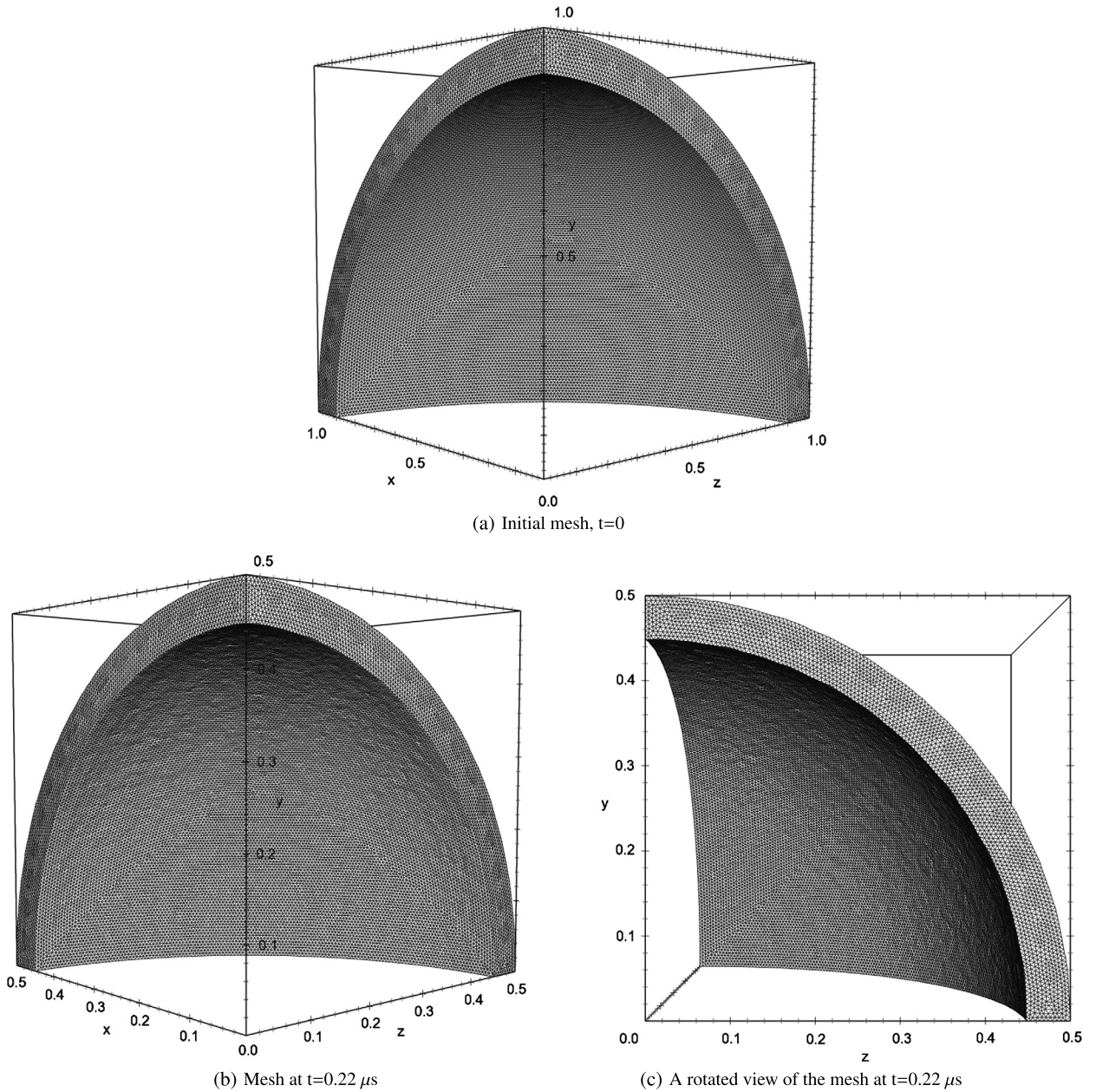


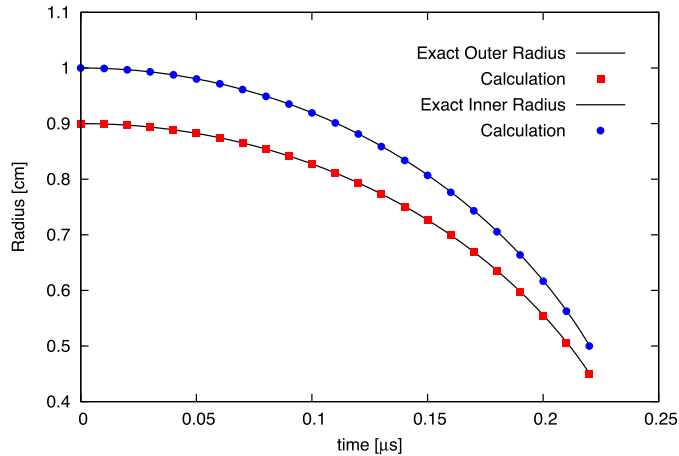
Fig. 22. The Kidder hollow shell test problem involves the isentropic compression of a shell of gas. The initial mesh is shown in the upper left corner. Two views of the final mesh are shown along the bottom row. The spatial scale goes from 0 to 1 cm in the initial mesh plot and from 0 to 0.5 cm in the final mesh plots, where the major spatial ticks are 0.1 cm in both plots. The initial and final thicknesses of the shell are 0.1 cm and 0.05 cm respectively. The mesh is smooth and symmetric. The surface radii are compared with the analytic solution in Fig. 23. Scatter plots are also provided in Fig. 23.

where τ is the focusing time, which is given by

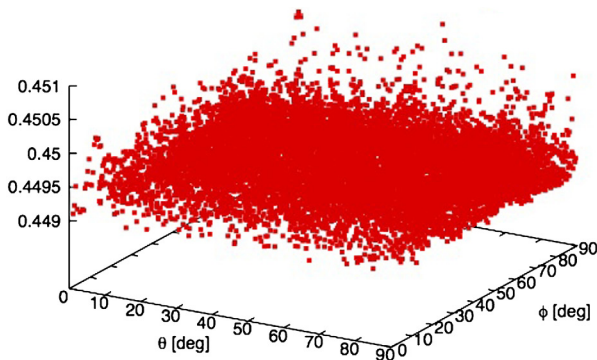
$$\tau = \sqrt{\frac{(\gamma - 1)(r_2^2 - r_1^2)}{2(c_2^2 - c_1^2)}} \tag{42}$$

The sound speed c is given by $c = \sqrt{\gamma \frac{p}{\rho}}$. The derivative with respect to time of the variable h is

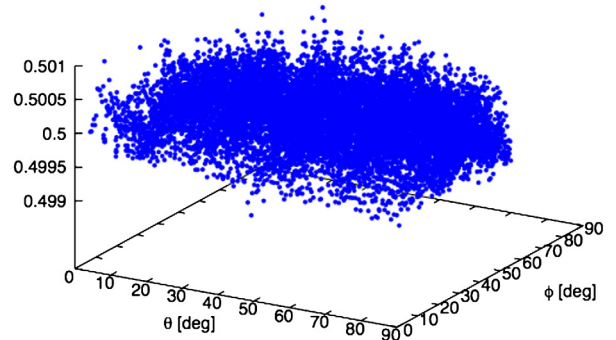
$$\frac{dh(t)}{dt} = \frac{t}{\tau^2} \frac{1}{h(t)} \tag{43}$$



(a) Comparison with the analytic solution



(b) Scatter plot of the inner surface radii at t=0.22



(c) Scatter plot of the outer surface radii at t=0.22

Fig. 23. The Kidder shell calculated results for the inner and outer radii are compared with the analytic solution every $0.01 \mu\text{s}$ in the top plot. The calculation closely follows the analytic solution. The bottom row provides scatter plots of the inner and outer radii as a function of the spherical coordinate angles θ and ϕ . The units for radii in the scatter plots are cm and the range is $\pm 0.001 \text{ cm}$, which is equal to $\pm 10 \mu\text{m}$. As demonstrated, the calculations are very symmetric and are in excellent agreement with the analytic solution.

The Kidder shell problem is calculated to a time of $t_{final} = \frac{\sqrt{3}}{2} \tau$, which corresponds to an inner and outer radius of 0.45 and 0.5 cm. The objective is to model the Kidder Shell problem as an initial value problem and use the surface radii of the shell to measure the accuracy of the hydrodynamic approach. As a result, the shell is compressed by initializing ghost regions adjacent to the inner and outer surfaces according to the initial profiles in Eq. (38). The exact solution as a function of time (Eq. (39)) is only applied to the free surfaces of the ghost regions and not on the shell boundaries, which allows numerical errors to manifest as deviations in the surface radii of the shell. All variables on the shell inner and outer surfaces solely evolve in time according to the numerical algorithm.

The mesh for this test problem is an octant of the entire shell with sliding boundary conditions along the $xy = 0$, $yz = 0$, and $xz = 0$ planes. The mesh is highly unstructured with an average edge length of 0.01 cm. The initial mesh and final mesh are shown in Fig. 22. The calculated radii are compared with the analytic solution in Fig. 23 every $0.01 \mu\text{s}$. The surface radii closely follow the exact solution. Scatter plots of the final inner and outer surface radii are provided in Fig. 23. The scatter plots show the radii vary less than $\pm 0.001 \text{ cm}$, which is equal to $\pm 10 \mu\text{m}$. The surfaces of the mesh are very symmetric and are in excellent agreement with the analytic solution.

8.7. Kidder sphere

The Kidder shell analytic solution in the previous subsection goes to infinity when the inner surface reaches the origin (e.g. Eq. (39) gives $\rho_1(0, \tau) = p_1(0, \tau) = u_1(0, \tau) = \infty$), so the accuracy of the ALE method was quantified on the implosion phase up to a time of $t_{final} = \frac{\sqrt{3}}{2} \tau$. Given this, we calculate another isentropic compression problem that is based on the work of Kidder and Coggeshall [12,50] that is valid for all time. This test problem is a sphere of gas that is isentropically compressed and is termed the Kidder sphere problem to delineate it from the Kidder shell problem in the previous subsection. The chief goal of the Kidder sphere test problem is to assess the ability of the hydrodynamic method to reach the theoretical maximum compression, which occurs at the origin. This test problem is isentropic so dissipation errors will artificially reduce the peak compression. Another goal is to demonstrate symmetry preservation. The equation

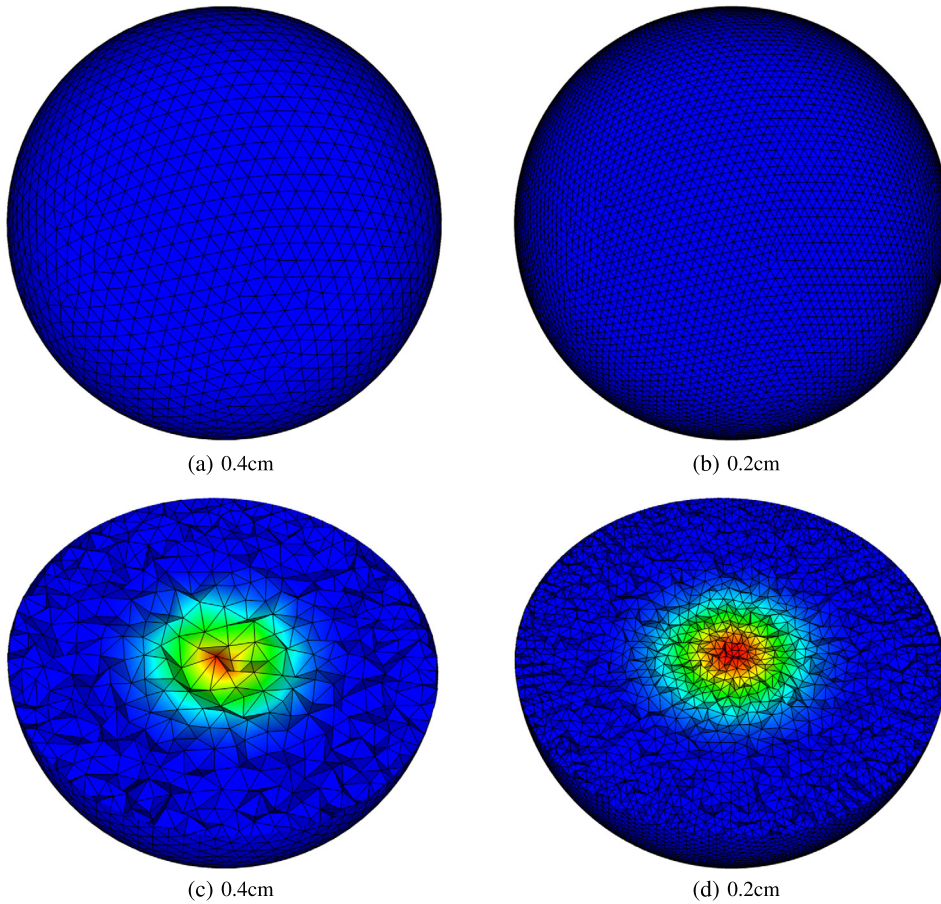


Fig. 24. The initial density field and the corresponding mesh is shown for the Kidder sphere problem. This test problem was calculated using a 3D unstructured tetrahedral mesh with three different resolutions – 0.4 cm, 0.3 cm, and 0.2 cm respectively. The entire, initial mesh is shown from the exterior in the top row, and the mesh is split open to show a slice through the center of the mesh in the second row.

of state is a gamma law gas with gamma equal to 5/3. The initial conditions of Kidder sphere test problem are as follows: an initial inward linear velocity profile, a Gaussian density profile, and a constant internal energy. The initial velocity profile is $u = -\frac{\sqrt{x^2+y^2+z^2}}{2}$, the initial density profile is $\rho = \frac{1}{\sqrt{2}} \exp\left(-\frac{x^2+y^2+z^2}{2}\right)$, and the initial internal energy is $\frac{3}{8}$. The analytic solution for the density, radial velocity, and specific internal energy is provided below as a function of time, t , and radius, r .

$$\begin{aligned} \rho &= 2\left(1 + (t - 1)^2\right)^{-\frac{3}{2}} \exp\left(-\frac{r^2}{1 + (t - 1)^2}\right) \\ u &= \frac{r(t - 1)}{1 + (t - 1)^2} \\ e &= \frac{\frac{3}{4}}{1 + (t - 1)^2} \end{aligned} \tag{44}$$

The units are g, cm, and μs . The radial velocity above is applied to the nodes on the outer surface, so this problem can be viewed as a spherical piston. The calculated solution will be compared to the analytic solution.

The problem is modeled using a 3D, highly unstructured tetrahedral mesh with three different mesh resolutions. The initial outer radius is 5 cm, and the initial mesh resolutions used for the convergence study are 0.04 cm, 0.03 cm, and 0.02 cm respectively. Slices through the initial meshes are provided in Fig. 24 to demonstrate the unstructured nature of the tetrahedral meshes. This problem is calculated using the ALE approach and the velocity smoothing settings are $c_1 = 1.0$ and $c_2 = 0.0$. The Laplacian (Eq. (30)) is solved until a tolerance of 0.1 is reached.

The density field along the center line of the mesh is shown in Fig. 25. As demonstrated, the density field is quite symmetric on this highly unstructured tetrahedral mesh. The scatter plots for density, pressure, and velocity are compared to the analytic solution at $t = 0.5 \mu\text{s}$ and at $t = 1.0 \mu\text{s}$ in Fig. 26. The peak compression occurs at $t = 1.0 \mu\text{s}$. The convergence

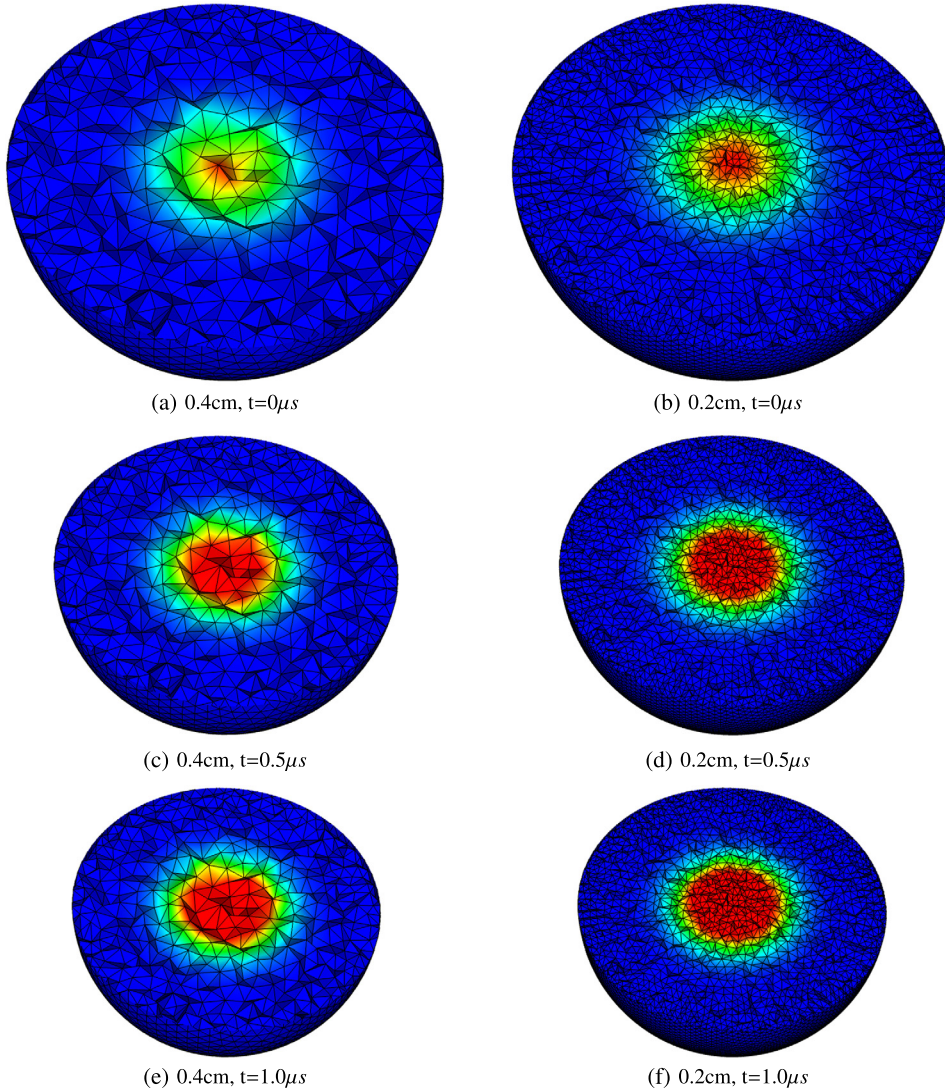


Fig. 25. The density field on a slice through the mesh is shown for the Kidder sphere problem at three times – $0 \mu\text{s}$, $0.5 \mu\text{s}$ and $1.0 \mu\text{s}$ respectively. The density scale is the same for all images and goes from 0 to 0.7 g/cc. The solution is very symmetric on this highly irregular mesh. The scatter plots are provided in Fig. 26, and the convergence plots are provided in Fig. 27.

plots for density and pressure are provided in Fig. 27 for $t = 0.5 \mu\text{s}$ and $t = 1.0 \mu\text{s}$. The ALE approach is converging at a rate slightly greater than 2. Furthermore, the magnitude of the L1 errors in both density and pressure are less than 0.001, which demonstrates that this algorithm is capable of calculating shock-free, smooth flows.

8.8. Taylor Green

The proposed PCH algorithm is primarily intended for flows with discontinuities; however, modeling smooth flows is still of value. The Taylor Green vortex problem is a shockless, smooth flow problem. The material is a gamma law gas, where $\gamma = 5/3$. The initial density is 1 g/cc. The initial velocity and pressure fields are

$$\begin{aligned}
 u^{t=0} &= \sin(\pi x) \cos(\pi y) \\
 v^{t=0} &= -\cos(\pi x) \sin(\pi y) \\
 w^{t=0} &= 0 \\
 p^{t=0} &= 10 + \frac{1}{4} (\cos(2\pi x) + \cos(2\pi y))
 \end{aligned} \tag{45}$$

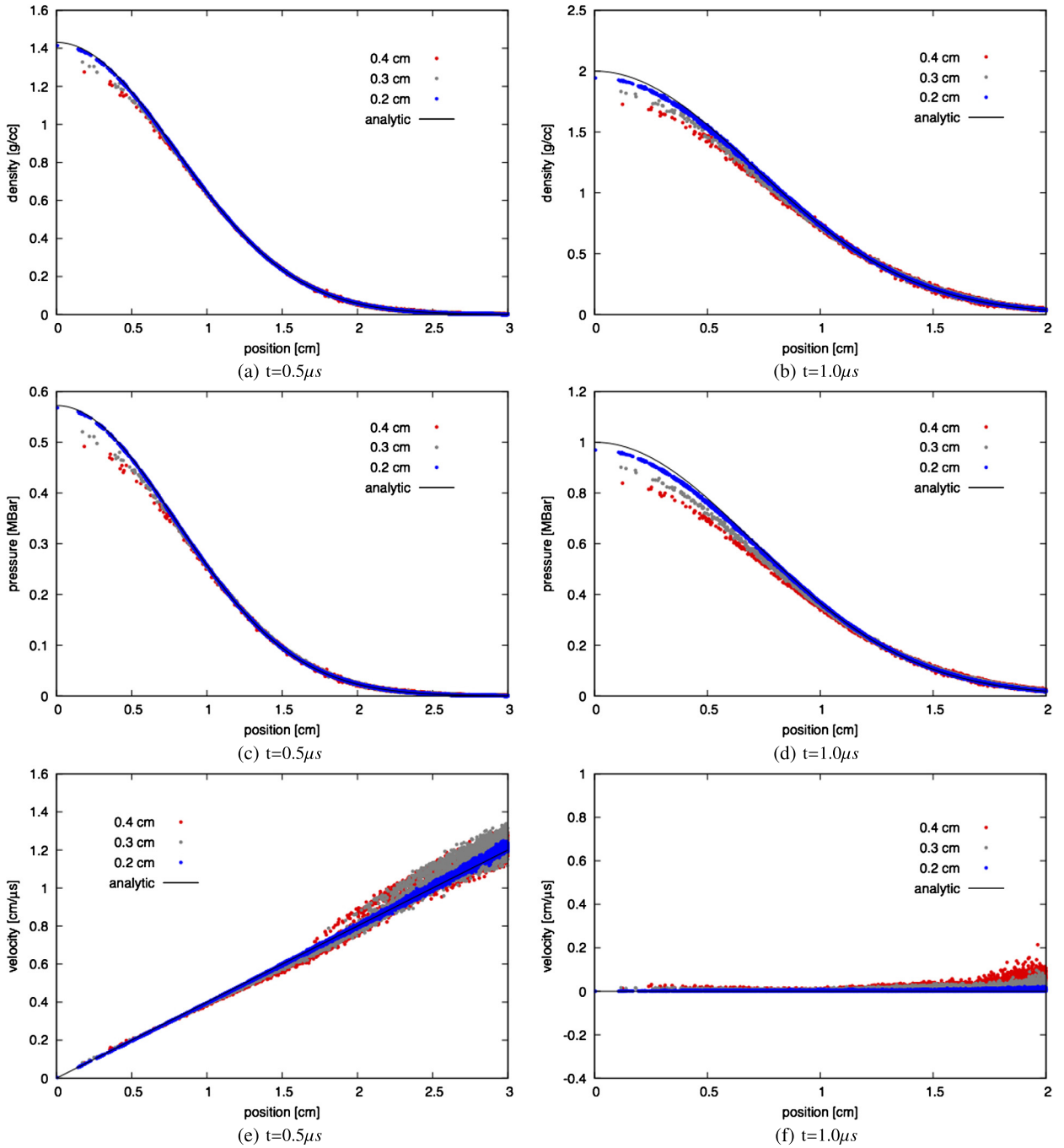


Fig. 26. The scatter plots for the Kidder sphere problem are shown corresponding to $t = 0.5 \mu s$ and $t = 1.0 \mu s$. The meshes used in this test are shown in the previous figure (Fig. 25). Every nodal value in the mesh is plotted. The velocity plot is the magnitude of the velocity vector at the node. As demonstrated, the results agree favorably with the analytic solution and the results improve with mesh refinement. The convergence plots are provided in Fig. 27.

An energy source term is included to maintain a steady state solution in the compressible inviscid case [18].

$$S_E = \frac{3\pi}{8} (\cos(\pi x) \cos(3\pi y) - \cos(3\pi x) \cos(y)) \tag{46}$$

Results are obtained in the ALE and Eulerian reference frames. The essentially Lagrangian results are provided in [46]. The computational meshes used here were created by decomposing a hexahedral mesh into 24 tetrahedra per hexahedron, which follows Lagrangian works in [53,46,68]. The domain is $1.0 \text{ cm} \times 1.0 \text{ cm}$ and the hexahedral mesh resolutions are

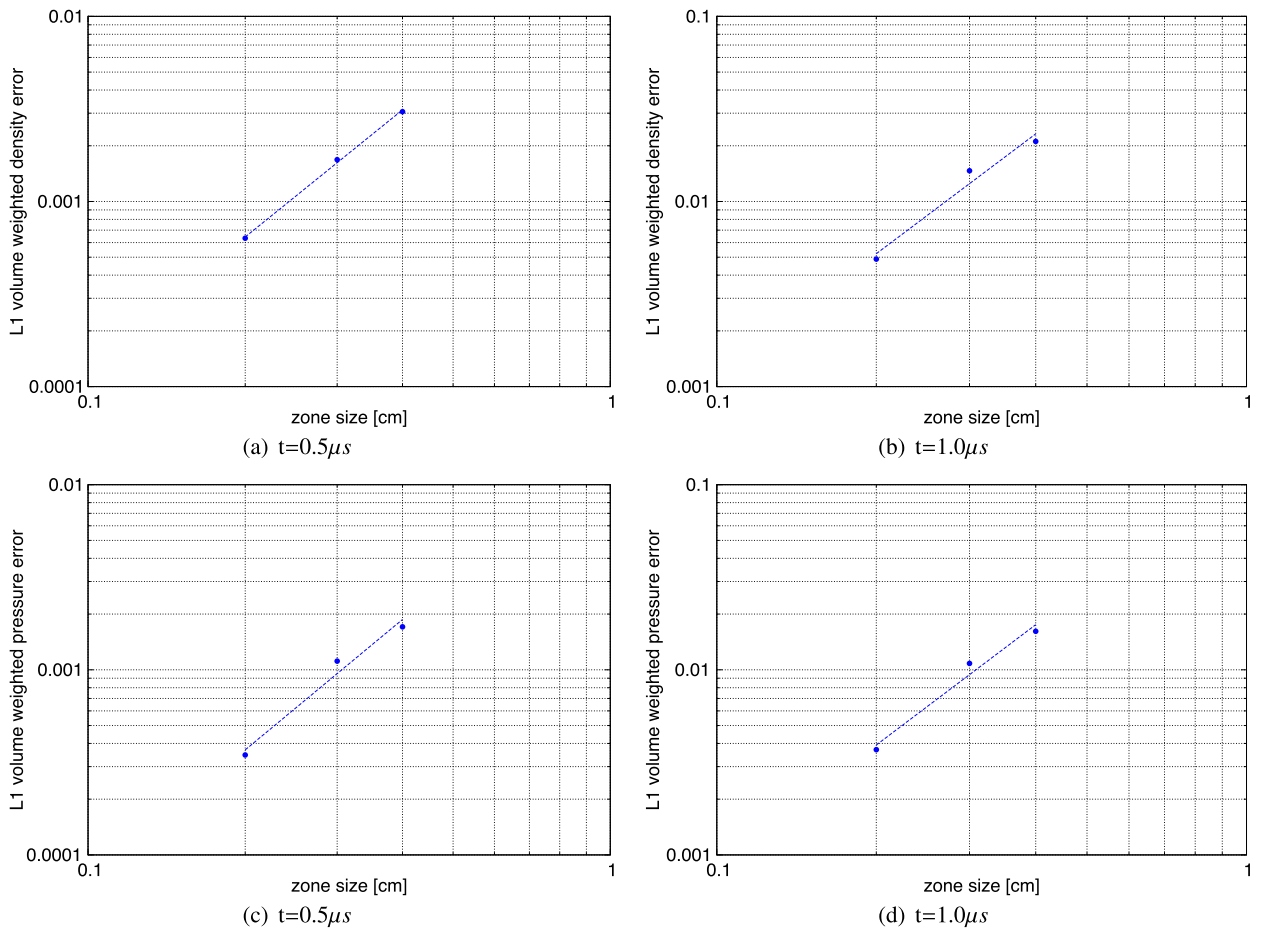


Fig. 27. The density and pressure convergence plots are shown for the Kidder sphere problem using the ALE approach. The errors are calculated using the nodal values in the mesh at a time of $0.5\ \mu s$ (left column) and $1.0\ \mu s$ (right column). For $t = 0.5\ \mu s$, the density errors are converging to zero at a rate of 2.28 and the power-law fit has an R^2 of 0.9991. The pressure errors are converging to zero at a rate of 2.34 and the power-law fit has an R^2 of 0.9864. Next, the density errors at $1.0\ \mu s$ are converging to zero at a rate of 2.15 and the power-law fit has an R^2 of 0.9831. The pressure errors at $1.0\ \mu s$ are converging to zero at a rate of 2.16 and the power-law fit has an R^2 of 0.9871.

$20 \times 20 \times 2$, $40 \times 40 \times 2$, and $80 \times 80 \times 2$. The depth of the computational mesh is chosen to make uniform hexahedral cells.

The Taylor Green vortex problem is of great value to this research effort because Lagrangian methods have difficulties calculating this test problem due to the severe mesh distortion [46]. The Lagrangian results shown in [46] correspond to a time of $0.5\ \mu s$, and there is already significant mesh deformation. To help illustrate the utility of the ALE approach, the Taylor Green vortex problem is calculated to a time of $1\ \mu s$. The mesh velocity smoothing parameters are $c_1 = 0.25$ and $c_2 = 0.25$. The Laplacian (Eq. (30)) is solved until a tolerance of 0.1 is reached.

The Taylor Green vortex results are shown in Figs. 28 and 29 corresponding to a time of $1\ \mu s$. The convergence plots are provided in Fig. 30. The velocity errors with the ALE approach and Eulerian approach are converging at a rate of 1.43 and 1.51 respectively. The new PCH ALE approach performs very well on this test problem.

8.9. Triple-point

The triple point problem is used to assess the robustness of the PCH ALE method on a problem that has significant vorticity, large shear, and complex interacting shocks [34]. The triple point problem is based on a similar test problem that was used by various Russian researchers to test hydrodynamic algorithms [56,58]. The triple point test problem has since been modeled by many ALE research efforts including [33,26,35,67,45]. The initial conditions are three regions of a gamma-law gas, where each region has a different initial condition. A region of high pressure drives a shock through two connected regions, which causes a vortex to develop at the triple point where the three regions connect. The initial conditions and dimensions for this problem are provided in Fig. 31. In this study, every region uses a gamma of 1.4. The initial mesh used for this test problem is unstructured and shown in Fig. 31. The mesh velocity smoothing parameters are

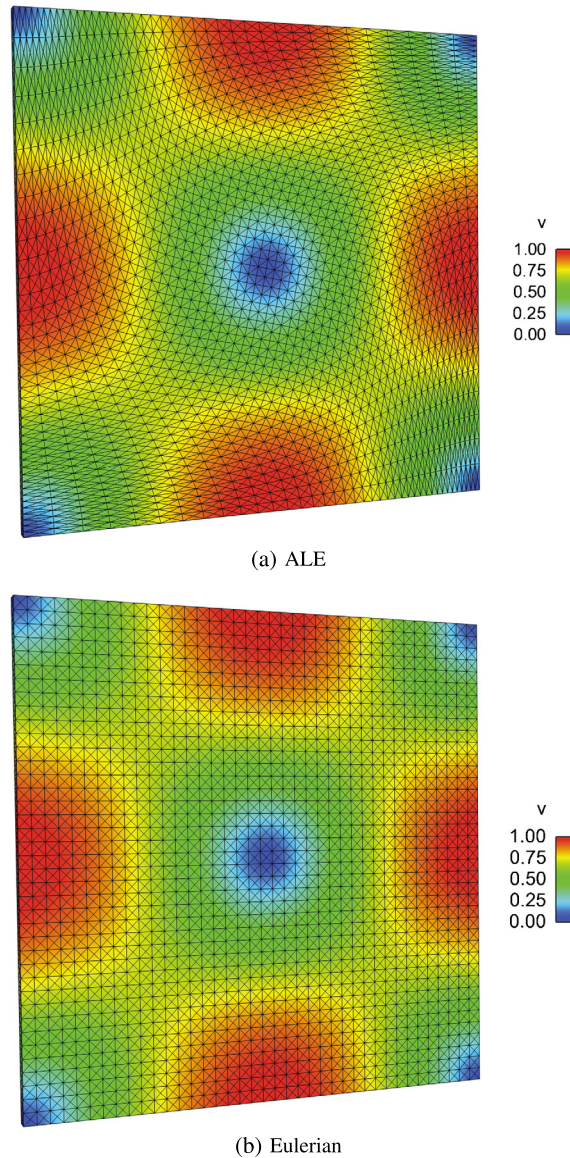


Fig. 28. The velocity field and the corresponding mesh for the Taylor Green problem is shown using the $40 \times 40 \times 2$ mesh. The results correspond to a time of $1 \mu\text{s}$. The ALE result is shown on the top and the Eulerian result is shown on the bottom. (For interpretation of the colors in this figure, the reader is referred to the web version of this article.)

$c_1 = 0.25$ and $c_2 = 0.5$. The Laplacian (Eq. (30)) is solved until a tolerance of 0.2 is reached. Fig. 32 shows the results at $5 \mu\text{s}$. As illustrated, the PCH ALE method is robust and able to model problems with complex flows.

9. Conclusion

A point centered hydrodynamic (PCH) arbitrary Lagrangian Eulerian (ALE) method was presented that is suitable for modeling complex flows on tetrahedral meshes. The PCH approach stores the conserved variables at the node and solves the governing equations on a control volume around the node, which is commonly termed the dual grid. The new PCH ALE approach solves a multidirectional approximate Riemann problem at the center of each tetrahedron; in addition, the advective and diffusive fluxes are calculated by solving a separate, 1D Riemann problem on each facet of the dual control volume. The solution is evolved forward in time by a two step Runge–Kutta method, where the advective fluxes are included in the time integration. The advective fluxes are a function of the difference between the mesh velocity and the fluid velocity. The mesh velocity will be equal to the fluid velocity in the Lagrangian limit so the advective fluxes are equal to zero. Next, the mesh velocity is equal to zero in the Eulerian limit. For the ALE case, the mesh

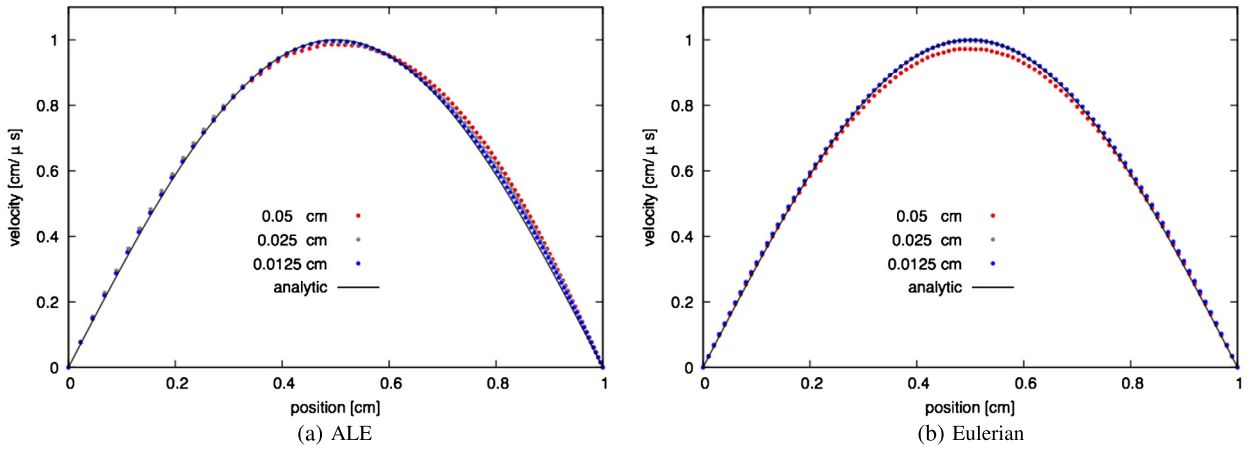


Fig. 29. The velocity at the nodes along a line through the mesh, near the bottom, is shown for the Taylor Green problem. The results correspond to a time of 1 μ s. The ALE result is shown on the top and the Eulerian result is shown on the bottom.

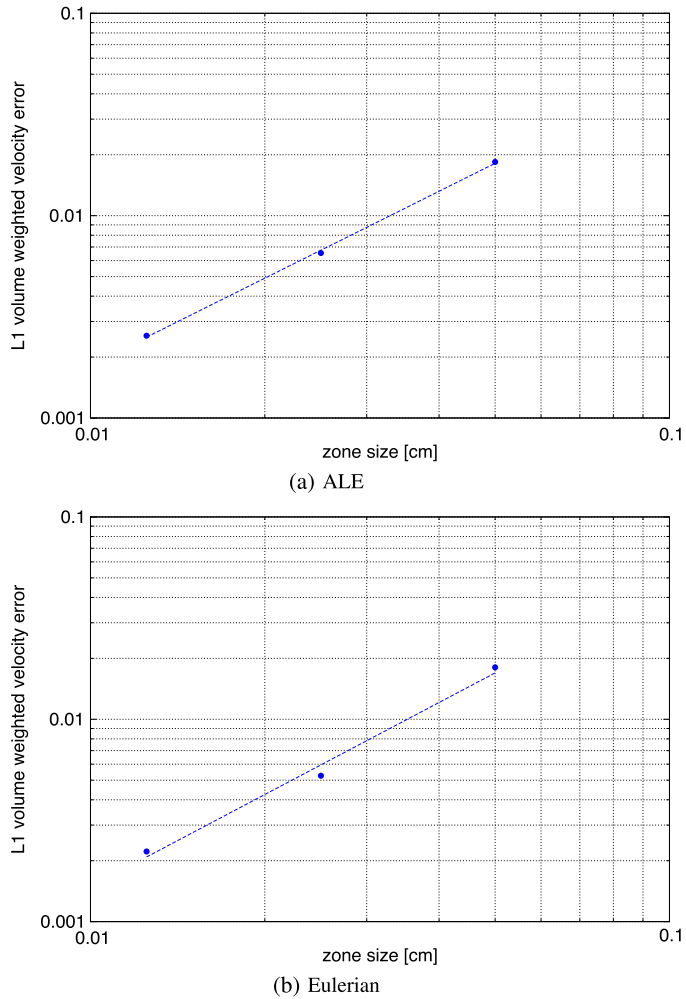


Fig. 30. Velocity convergence plots are shown for the Taylor Green problem using the ALE and Eulerian approaches. The errors are calculated using every nodal value in the mesh at a time of 1 μ s. The density errors with the ALE approach are converging to zero at a rate of 1.43 and the power-law fit has an R^2 of 0.9996. Next, the density errors with the Eulerian approach are converging to zero at a rate of 1.511 and the power-law fit has an R^2 of 0.9948.

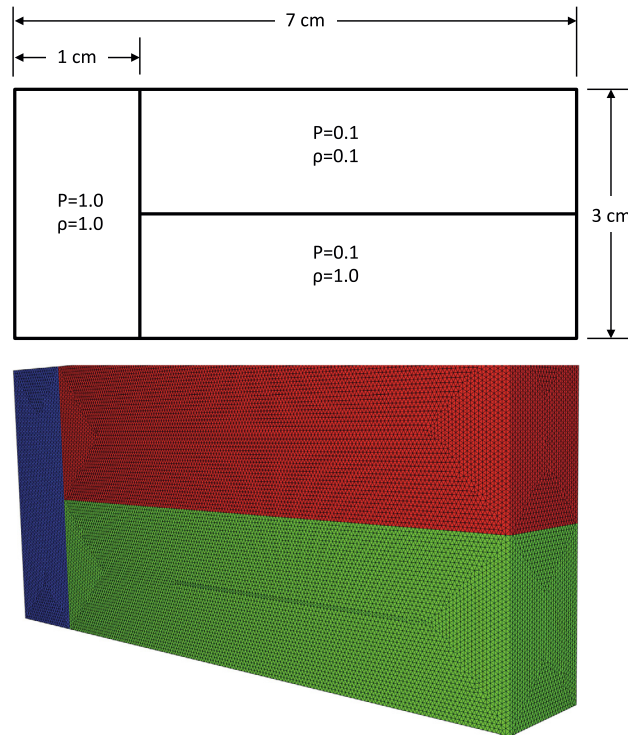


Fig. 31. The initial setup and mesh for the Triple point problem is shown.

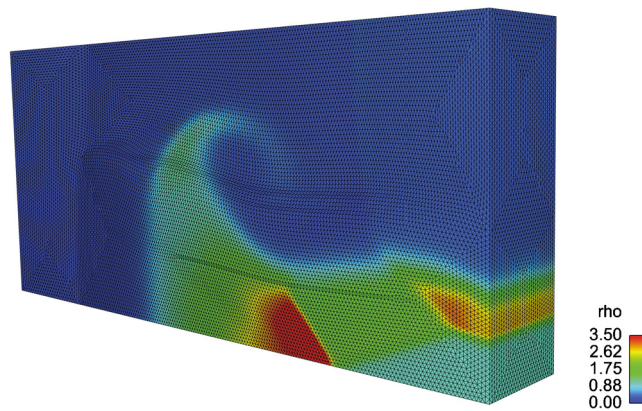


Fig. 32. The density and corresponding mesh for the triple point problem at 5 μ s is shown. (For interpretation of the colors in this figure, the reader is referred to the web version of this article.)

velocity is smoothed by solving a Laplacian equation, where the initial mesh velocity is a function of the fluid velocity.

The new PCH ALE algorithm produces excellent results on a range of test problems using tetrahedral meshes. The ALE algorithm was evaluated in the Eulerian limit and with arbitrary mesh velocities. The results from this algorithm in the Lagrangian limit are presented in [46]. The test problems used in this work were the Geometric conservation law (GCL), Sod, Sedov XY, Sedov XYZ, Saltzman, Kidder, Taylor Green vortex, and triple-point. The GCL problem was used to quantify volume errors in the ALE approach. An unstructured tetrahedral mesh was used with the GCL problem. The volume errors associated with the GCL were shown to be very small and converge toward zero at a rate of about 2.8. Next, the Sod test problem was used to demonstrate the ability of the ALE and Eulerian approaches to accurately propagate a release wave away from a contact discontinuity and transmit a shock. An unstructured mesh was used with Sod. The Sod results were symmetric and agreed well with the analytic solution. The errors in the density and pressure fields were converging at a rate of 0.72 and 0.77 respectively for the ALE approach. Likewise, the errors in the density and pressure are converging at a rate of 0.74 and 0.82 respectively with the Eulerian approach. Next, the Sedov problem is a blast wave in a gas and it was used to demonstrate the accuracy of the ALE and Eulerian methods at converting internal energy into kinetic energy.

Several different tetrahedral mesh topologies were used on the Sedov problems including highly unstructured meshes. The density errors were converging at a rate of 0.87 for the ALE approach and 0.82 for the Eulerian approach. Next, the Saltzman problem was calculated using ALE to demonstrate the robustness of the approach. The Saltzman problem has an initially skewed mesh that creates challenges for hydrodynamic methods. Favorable results were presented before and after the shock reflected from the wall on the Saltzman problem. Next, two isentropic compression problems were calculated, which are called the Kidder shell and Kidder sphere test problems. These isentropic compression test problems were used to test the accuracy of the ALE approach on smooth flows. The calculated results on the Kidder problems demonstrate this hydrodynamic approach is very accurate with minimal dissipation errors. The radii of the surfaces in the Kidder shell test problem were in excellent agreement with the analytic solution. Likewise, the density and pressure errors are converging to zero at a rate slightly greater than 2 on the Kidder sphere problem. Next, the Taylor Green vortex problem and the triple point problem were used to test the robustness and the accuracy of the ALE approach on a problem with vorticity. The velocity errors on the Taylor Green vortex problem were small and converging at a rate of 1.43 with the ALE approach and 1.51 with the Eulerian approach. The last test was the triple-point problem, which was used to test the ALE approach on a more complex problem that has significant vorticity and shear combined with more complex shock interactions. As demonstrated in this work and similar works [67,5], ALE algorithms can be derived that are suitable for modeling shock problems on tetrahedral meshes.

Acknowledgements

We would like to thank L. Dean Risinger for developing data structures for unstructured tetrahedral meshes. We are grateful for the help from Scott Ramsey on the Kidder problems. We also gratefully acknowledge the support of the NNSA through the Laboratory Directed Research and Development program at Los Alamos National Laboratory. The Los Alamos unlimited release number is LA-UR-14-26454.

References

- [1] F. Addessio, J. Baumgardner, J. Dukowicz, N. Johnson, B. Kashiwa, R. Rauenzahn, C. Zemach, CAVEAT: a computer code for fluid dynamics problems with large distortion and internal slip, Technical Report LA-10613-MS-REV.1, Los Alamos National Laboratory, 1990.
- [2] F. Addessio, M. Cline, J. Dukowicz, A general topology, Godunov method, *Comput. Phys. Commun.* 48 (1988) 65–73.
- [3] T. Barth, An introduction to recent developments in theory and numerics for conservation laws, in: C. Rohde, D. Kroner, M. Ohlberger (Eds.), *Lecture Notes in Computational Science and Engineering*, Springer, 1998, pp. 274–275.
- [4] W. Boscheri, D.S. Balsara, M. Dumbser, High-order Lagrangian ADER–WENO finite volume schemes on unstructured triangular meshes based on genuinely multidimensional HLL Riemann solvers, *J. Comput. Phys.* 267 (2014) 112–138.
- [5] W. Boscheri, M. Dumbser, A direct arbitrary-Lagrangian–Eulerian ADER–WENO finite volume scheme on unstructured tetrahedral meshes for conservative and non-conservative hyperbolic systems in 3D, *J. Comput. Phys.* 275 (2014) 484–523.
- [6] D. Burton, Multidimensional discretization of conservation laws for unstructured polyhedral grids, Technical Report UCRL-JC-118306, Lawrence Livermore National Laboratory, 1994.
- [7] D. Burton, T. Carney, N. Morgan, S. Sambasivan, M. Shashkov, A cell centered Lagrangian Godunov-like method of solid dynamics, *J. Comput. Fluids* 83 (2013) 33–47.
- [8] E. Caramana, D. Burton, M. Shashkov, P.P. Whalen, The construction of compatible hydrodynamic algorithms utilizing conservation of total energy, *J. Appl. Phys.* 146 (1998) 227–262.
- [9] E. Caramana, C. Rousculp, D. Burton, A compatible energy and symmetry preserving Lagrangian hydrodynamics algorithm in three dimensional Cartesian geometry, *J. Comput. Phys.* 157 (2000) 89–119.
- [10] G. Carré, S. Del Pino, B. Després, E. Labourasse, Cell-centered Lagrangian hydrodynamics scheme on general unstructured meshes in arbitrary dimension, *J. Comput. Phys.* 228 (2009) 5160–5183.
- [11] R. Clark, The evolution of HOB0, *Comput. Phys. Commun.* 48 (1988) 61–64.
- [12] S. Coggeshall, Analytic solutions of hydrodynamics equations, *Phys. Fluids A* 3 (1991) 760–769.
- [13] P. Cooper, *Explosive Engineering*, Wiley-VCH, 1996, pp. 188–189.
- [14] W. Crowley, *Proceedings of the Second International Conference on Numerical Methods in Fluid Dynamics*, Springer-Verlag, 1971.
- [15] W. Crowley, Free-Lagrangian methods for compressible hydrodynamics in two space dimensions, in: *Proceedings of the First International Conference on Free-Lagrange Methods*, Springer-Verlag, 1985, pp. 1–21.
- [16] S. Davis, Simplified second-order Godunov-type methods, *SIAM J. Sci. Stat. Comput.* 3 (1988) 445–473.
- [17] B. Després, C. Mazeran, Lagrangian gas dynamics in two dimensions and Lagrangian systems, *Arch. Ration. Mech. Anal.* 178 (2005) 327–372.
- [18] V. Dobrev, T. Ellis, T. Kolev, R. Rieben, Curvilinear finite elements for Lagrangian hydrodynamics, *Int. J. Numer. Methods Fluids* 65 (2011) 1295–1310.
- [19] S. Doebling, Impact of numerical treatment of shocks on verification assessment of the FLAG Lagrangian hydrodynamics code using the Sedov problem, Technical Report, Los Alamos National Laboratory, 2014.
- [20] J. Dukowicz, A general, non-iterative Riemann solver for Godunov’s method, *J. Comput. Phys.* 61 (1985) 119–137.
- [21] J. Dukowicz, B. Meltz, Vorticity errors in multidimensional Lagrangian codes, *J. Comput. Phys.* 99 (1992) 115–134.
- [22] M. Esmond, A. Thurber, One dimensional Lagrangian hydrocode development, Technical Report LA-UR-13-26506, Los Alamos National Laboratory, 2013.
- [23] C. Farhat, P. Geuzine, C. Grandmont, The discrete geometric conservation law and the nonlinear stability of ALE schemes for the solution of flow problems on moving grids, *J. Comput. Phys.* 174 (2001) 669–694.
- [24] L. Formaggia, J. Peraire, K. Morgan, Simulation of store separation using the finite element method, *Appl. Math. Model.* 12 (1988) 175–181.
- [25] M. Fritts, J. Boris, The Lagrangian solution of transient problems in hydrodynamics using a triangular mesh, *J. Comput. Phys.* 31 (1979) 173–215.
- [26] S. Galera, P.-H. Maire, J. Breil, A two-dimensional unstructured cell-centered multi-material ALE scheme using VOF interface reconstruction, *J. Comput. Phys.* 229 (2010) 5755–5787.
- [27] M. Gittings, Trix: a free-Lagrangian hydrocode, in: *Proceedings of the Advances in the Free-Lagrange Method conference*, Springer-Verlag, 1990, pp. 28–36.
- [28] H. Guillard, C. Farhat, On the significance of the geometric conservation law for flow computations on moving meshes, *Comput. Methods Appl. Mech. Eng.* 190 (2000) 1467–1482.

- [29] F. Harlow, Hydrodynamic problems involving large fluid distortions, *J. Assoc. Comput. Mach.* 4 (1957) 137–142.
- [30] R. Kidder, Laser compression of matter: optical power and energy requirements, *Nucl. Fusion* 14 (1974) 797–803.
- [31] R. Kidder, Theory of homogeneous isentropic compression and its application to laser fusion, *Nucl. Fusion* 14 (1974) 53–60.
- [32] R. Kidder, Laser-driven compression of hollow shells: power requirements and stability limitations, *Nucl. Fusion* 16 (1976) 3–14.
- [33] M. Kucharik, R. Garimella, S. Schofield, M. Shashkov, A comparative study of interface reconstruction methods for multi-material ale simulations, *J. Comput. Phys.* 229 (2010) 2432–2452.
- [34] R. Loubère, Validation test case suite for compressible hydrodynamics computation, Technical Report, Los Alamos National Laboratory, 2005.
- [35] R. Loubère, P.-H. Maire, M. Shashkov, J. Breil, S. Galera, ReALE: a reconnection-based arbitrary Lagrangian Eulerian method, *J. Comput. Phys.* 229 (2010) 4724–4761.
- [36] R. Loubère, P.-H. Maire, P. Váchal, Formulation of a staggered two-dimensional Lagrangian scheme by means of cell-centered approximately Riemann solver, *Numer. Math. Adv. Appl.* (2009) 617–625.
- [37] R. Loubère, P.-H. Maire, P. Váchal, A second-order compatible staggered Lagrangian hydrodynamics scheme using a cell-centered multidirectional Riemann solver, *Proc. Comput. Sci.* 1 (2010) 1925–1933.
- [38] R. Loubère, P.-H. Maire, P. Váchal, 3D staggered Lagrangian hydrodynamics with cell-centered Riemann solver-based artificial viscosity, *Int. J. Numer. Methods Fluids* 72 (2013) 22–42.
- [39] P.-H. Maire, A high-order cell-centered Lagrangian scheme for two-dimensional compressible fluid flows on unstructured mesh, *J. Comput. Phys.* 228 (2009) 2391–2425.
- [40] P.-H. Maire, R. Abgrall, J. Breil, J. Ovadia, A cell-centered Lagrangian scheme for two-dimensional compressible flow problems, *SIAM J. Sci. Comput.* 29 (2007) 1781–1824.
- [41] P.-H. Maire, R. Loubère, P. Vachal, Staggered Lagrangian discretization based on cell-centered Riemann solver and associated hydrodynamics scheme, *Commun. Comput. Phys.* 10 (2011) 940–978.
- [42] L. Margolin, A centered artificial viscosity for cells with large aspect ratios, Technical Report UCRL-S3882, Los Alamos National Laboratory, 1988.
- [43] S. Marsh, LASL Shock Hugoniot Data, University of California Press, 1980.
- [44] N. Morgan, M. Kenamond, D. Burton, T. Carney, D. Ingraham, A contact surface algorithm for cell-centered Lagrangian hydrodynamics, *J. Comput. Phys.* 250 (2013) 527–554.
- [45] N. Morgan, K. Lipnikov, D. Burton, M. Kenamond, A Lagrangian staggered grid Godunov-like approach for hydrodynamics, *J. Comput. Phys.* 259 (2014) 568–597.
- [46] N. Morgan, J. Waltz, D. Burton, M. Charest, T. Canfield, J. Wohlbier, A Godunov-like point-centered essentially Lagrangian hydrodynamic approach, *J. Comput. Phys.* 281 (2014) 614–652.
- [47] S. Murman, M. Aftosmis, M. Berger, Simulations of 6-dof Motion with a Cartesian Method, in: 41st AIAA Aerospace Sciences Meeting, AIAA-2003-1246, Reno, NV, 2003.
- [48] V.-T. Nguyen, An arbitrary Lagrangian–Eulerian discontinuous Galerkin method for simulations of flows over variable geometries, *J. Fluids Struct.* 26 (2010) 312–329.
- [49] B. Nkonga, H. Guillard, Godunov type method on non-structured meshes for three-dimensional moving boundary problem, *Comput. Methods Appl. Mech. Eng.* 113 (1994) 183–204.
- [50] S. Ramsey, A class of self-similar hydrodynamic test problems, Technical Report LA-UR-10-08184, Los Alamos National Laboratory, 2010.
- [51] R. Rausch, J. Batina, H. Yang, Three-dimensional time-marching aeroelastic analyses using an unstructured-grid Euler method, *AIAA J.* 31 (1993) 1626–1633.
- [52] M. Sahota, An explicit–implicit solution of the hydrodynamic and radiation equations, in: *Proceedings of the Advances in the Free-Lagrange Method Conference*, Springer-Verlag, 1990, pp. 28–36.
- [53] G. Scovazzi, Lagrangian shock hydrodynamics on tetrahedral meshes: a stable and accurate variational multi scale approach, *J. Comput. Phys.* 231 (2013) 8029–8069.
- [54] G. Scovazzi, J. Shadid, E. Love, W. Rider, A conservative nodal variational multiscale method for Lagrangian shock hydrodynamics, *Comput. Methods Appl. Mech. Eng.* 199 (2010) 3059–3100.
- [55] L. Sedov, *Similarity and Dimensional Methods in Mechanics*, Academic Press, 1959, p. 146.
- [56] M. Shashkov, A. Solovjov, Numerical simulation of two-dimensional flows by the free-Lagrangian method, Technical Report TUM-M9105, Technische Universität München, 1991.
- [57] G. Sod, A survey of several finite difference methods for systems of non-linear hyperbolic conservation laws, *J. Comput. Phys.* 27 (1978) 1–31.
- [58] I. Sofonov, V. Rasskazova, L. Nexterenko, The use of nonregular nets for solving two-dimensional non-stationary problems in gas dynamics, in: N. Yenenko, Yu. Shokin (Eds.), *Numerical Methods in Fluid Dynamics*, Mir, Moscow, 1984, pp. 82–121.
- [59] P.D. Thomas, C.K. Lombard, Geometric conservation law and its application to flow computations on moving grids, *AIAA J.* 17 (1979) 1030–1037.
- [60] V. Venkatakrishnan, Convergence to steady state solutions of the Euler equations on unstructured grids with limiters, *J. Comput. Phys.* 118 (1995) 120–130.
- [61] F. Vilar, P.-H. Maire, R. Abgrall, A discontinuous Galerkin discretization for solving the two-dimensional gas dynamics equations written under total Lagrangian formulation on general unstructured grids, *J. Comput. Phys.* 276 (2014) 188–234.
- [62] J. von Neumann, R. Richtmyer, A method for the calculation of hydrodynamics shocks, *J. Appl. Phys.* 21 (1950) 232–237.
- [63] J. Waltz, Derived data structure algorithms for unstructured finite element meshes, *Int. J. Numer. Methods Eng.* 54 (2002) 945–963.
- [64] J. Waltz, Microfluidics simulation using adaptive unstructured grids, *Int. J. Numer. Methods Fluids* 46 (2004) 939–960.
- [65] J. Waltz, Operator splitting and time accuracy in Lagrange plus remap solution methods, *J. Comput. Phys.* 253 (2013) 247–258.
- [66] J. Waltz, T. Canfield, N. Morgan, L. Risinger, J. Wohlbier, Verification of a three-dimensional unstructured finite element method using analytic and manufactured solutions, *Comput. Fluids* 81 (2013) 57–67.
- [67] J. Waltz, N. Morgan, T. Canfield, M. Charest, J. Wohlbier, A three-dimensional finite element arbitrary Lagrangian–Eulerian method for shock hydrodynamics on unstructured grids, *Comput. Fluids* 92 (2013) 172–187.
- [68] J. Waltz, N. Morgan, T. Canfield, M. Charest, J. Wohlbier, A nodal Godunov method for Lagrangian shock hydrodynamics on unstructured tetrahedral grids, *Int. J. Numer. Methods Fluids* (2014), <http://dx.doi.org/10.1002/fld.3928>, in press.
- [69] J. Waltz, J. Wohlbier, L. Risinger, T. Canfield, M. Charest, A. Long, N. Morgan, Performance analysis of a 3D unstructured hydrodynamics code on multi-core and many-core architectures, *Int. J. Numer. Methods Fluids* (2014), <http://dx.doi.org/10.1002/fld.3982>, in press.
- [70] M. Wilkins, Use of artificial viscosity in multidimensional shock wave problems, *J. Comput. Phys.* 36 (1980) 281–303.
- [71] H. Zhang, M. Reggio, J.Y. Trepánier, R. Camareo, Discrete forms of the GCL for moving meshes and its implementation in CFD schemes, *Comput. Fluids* 22 (1993) 9–23.
- [72] J. Zukas, W. Walters, *Explosive Effects and Applications*, Springer, 1998, p. 105.